Linear trends of temperature, salinity, and oxygen in the North Pacific based on GOBAI-O_2 over 2 decades and their controlling factors

Miho Ishizu[1, 2], Tomomichi Ogata[3]

[1]*Center for Climate Physics, Institute for Basic Science, Busan 46241, Republic of Korea*
[2]*Pusan National University, Tonghapgigyegwan Bldg 2 Busandaehak-ro, 63 beon-gil, Geumjeong-gu, Busan 46241, Republic of Korea*
[3]*Japan Agency for Marine-Earth Science and Technology, Environmental Variability Prediction and Application Research Group, Yokohama Institute for Earth Sciences, 3173-25 Showa-machi, Kanagawa-ku, Yokohama 236-0001, Japan*

To whom correspondence may be addressed. Email: mishizu@pusan.ac.kr

Abstract

Oxygen concentrations in the ocean are believed to be declining due to global warming. However, our understanding of its variability remains limited compared to physical parameters such as temperature and salinity, because oxygen is difficult to observe with high spatial and temporal resolution. In this study, we analyzed linear trends in potential temperature, salinity, and dissolved oxygen in the North Pacific over the past two decades (2004–2023), using the GOBAI-O_2 data. We then compared oxygen trends with physical parameters to investigate the spatial pattern of linear changes across the region. The oxygen trends derived from GOBAI-O_2 were consistent with those observed along hydrographic lines that have been relatively frequently and continuously surveyed by ship-based observations. Although an overall declining trend in dissolved oxygen was evident, localized increases were observed in certain density layers. By examining the associated physical conditions, we found that the spatial heterogeneity of the oxygen trends can be attributed to known oceanographic processes, such

as the southward retreat of the oxygen minimum layer and the northward migration of a recently identified front separating the subtropical and subarctic gyres. Our findings highlight the utility of GOBAI-O_2 data in linking physical changes to previously unrecognized biological and biogeochemical patterns in the ocean.

Plain Language Summary

1. We examined the linear trends in potential water temperature, salinity, and dissolved oxygen in the North Pacific over the past 20 years using GOBAI-O_2 data and explored the mechanisms behind these trends.
2. Our findings confirmed that the observed trends are consistent with findings from previous studies and further revealed spatial trend linkages that had only been partially recognized.
3. The results showed an overall decreasing trend in oxygen, although some localized regions exhibited an increasing trend, indicating the fluctuations were not uniform in the North Pacific. The spatial non-uniformity was explained by the background of physical phenomena. In particular, the oxygen increase in the northern North Pacific was attributed to the northern meridional shift of the front between the subtropical and subarctic gyres. Meanwhile, the retreat of the westward penetration of the oxygen minimum layer in the equatorial area was associated with a weakening and poleward shift of the NECC on interdecadal variability.
4. The result of this study provides one of the pieces of evidence linking physical changes to previously unclear changes in biological observations.

Keywords: dissolved oxygen, 20-year linear trends, Bio-Argo float data, global warming

1. Introduction

Recent decades have witnessed a reduction in the global ocean's dissolved oxygen inventory, a trend that is projected to continue over the course of the 21th century [Keeling et al., 2010; Breitburg et al., 2018; Stramma and Schmidtko, 2021; Limburg et al., 2020; Ito et al. 2017, 2024; Kolodziejczyk et al. 2024]. This decline is attributed to the release of oxygen from the ocean due to oxygen solubility resulting from rising surface temperatures. Additionally, enhanced stratification and stagnation of ocean circulation caused by global warming are also contributing factors [Keeling et al., 2010, Bopp et al. 2013; Ito et al. 2017]. Oxygen outgassing can have harmful effects on aerobic marine organisms [Pörtner and Farrell, 2008; Sampaio et al., 2021] and may alter biogeochemical cycles and trigger important climatological feedback [Berman-Frank et al., 2008]. Historical deoxygenation has been inferred from analyses of globally distributed observation data [Helm et al., 2011; Schmidtko et al., 2017; Ito et al., 2017; Takatani et al., 2012; Sasano et al., 2015; Lauvset et al., 2022b]. Earth system models have been used to simulate historical and projected future deoxygenations of the oceans [Bopp et al., 2013; Kwiatkowski et al., 2020; Li et al. 2020].

Oxygen trends have been observed and discussed using the discrete measurements of dissolved oxygen concentration (O_2). These measurements are usually made by Winker titration [Winkler, 1988]. These titrations are also used to calibrate the readings of electrode (or more recently optical) dissolved oxygen sensors attached to conductivity-water temperature-depth (CTD) profilers [Helm et al. 2011; Schmidtko et al., 2017; Lauvset et al., 2022b]. In the WOCE, CLIVAR, and GO-SHIP programs, oxygen data have been collected globally using this approach, but their temporal resolution is on the order of ten years, which does not allow for a robust analysis of annual or seasonal variations in dissolved oxygen (O_2). Some dissolved O_2 data are relatively frequently observed in a specific local area during a year [Takatani et al. 2012, Sasano et al., 2015], but they are localized, and so it is difficult to know how the phenomena are connected or disconnected each other, although some

76 research did the trials to understand the spatial variability of dissolved O_2 [Ito et al. 2017; Stramma et
77 al. 2020; Kolodziejczyk et al. 2024]. Therefore, we must have a very limited spatial-temporal
78 understanding of the observed data in dissolved oxygen.

79

80 Oxygen sensors were first installed on Argo profiling floats in the mid-2000s, and since then,
81 approximately 1,800 of these floats, equipped with oxygen sensors, have been deployed in the ocean
82 around the world, advancing efforts to deepen our understanding of trends and variability in oceanic
83 oxygen levels [Sharp et al., 2023]. The effort to establish a global biogeochemical Argo network has
84 led to the deployment of oxygen-sensor-equipped Argo floats in regions of the ocean that were
85 previously less sampled [Claustre et al., 2020]. As the number of deployed floats has grown,
86 significant progress has been made in sensor calibration, data adjustments, and quality control.
87 Noteworthy improvements include pre-deployment drift corrections [D'Asaro and McNeil, 2013;
88 Johnson et al., 2015; Bittig and Körtzinger, 2015; Bushinsky et al., 2016; Drucker and Riser, 2016;
89 Nicholson and Feen, 2017], climatology-based calibrations [Takeshita et al., 2013], in-air oxygen
90 measurement calibrations [Körtzinger et al., 2005; Bittig and Körtzinger, 2015; Johnson et al., 2015;
91 Bushinsky et al., 2016], post-deployment drift corrections [Johnson et al., 2017; Bittig et al., 2018a,
92 b], and the development of procedures for delayed-mode quality control [Maurer et al., 2021]. These
93 advancements have significantly reduced measurement uncertainty and improved the consistency of
94 optode-based [O_2] measurements from Argo floats.

95

96 Measurement data from oxygen sensors installed on the Argo float have primarily been used for
97 localized process studies. Specially, these studies have focused on air-sea oxygen exchange [Wolf et
98 al., 2018], upper-ocean primary production [Alkire et al., 2012; Estapa et al., 2019], the efficiency
99 of the biological pump [Johnson and Bif, 2021], and the dynamics of the oxygen minimum zone

100 [Udaya Bhaskar et al., 2021].

101

102 Sharp et al. [2023] recently produced a four-dimensional gridded [O_2] product, called GOBAI-O_2
103 (Gridded Ocean Biogeochemistry from Artificial Intelligence (AI) – Oxygen). GOBAI-O_2 is
104 developed using machine learning (ML), a subfield of AI that specializes in training, understanding,
105 and applying algorithms that learn and reproduce patterns artificially using data. Their analysis shows
106 the possibility that the GOBAI-O_2 data may reveal spatial patterns, seasonal cycles, and decadal
107 variability, with particular emphasis on the potential for these data to serve as valuable new
108 observational assets in areas where observational data gaps and high background O_2 variability overlap.

109

110 Regarding the O_2 trends in the North Pacific, Ito et al. [2017] used the objectively mapped monthly
111 climatology of O_2 based on the World Ocean Database 2013 (WOD13) [Boyer et al., 2013] at standard
112 depths from 1958 to 2015 and found multidecadal trends and variability in dissolved O_2 in the surface
113 layer. Sasano et al. [2015] detected significant warming trends and circulation changes by using the
114 JMA's high-frequency shipboard observational sections along the 137°E and 165°E lines from 1987
115 to 2011 in the western North Pacific. Their results showed that the O_2 declines in the northern
116 subtropical to subtropical-subarctic transition zones averaged -0.45 ± 0.16 μmol/kg/yr at 25.3 σ_θ and -
117 0.45 ± 0.14 μmol/kg/yr at 26.8 σ_θ, respectively. A significant positive trend in dissolved O_2 was
118 detected in the tropical Oxygen Minimum Layer (OML), with an increase of +0.36 ± 0.004 μmol/kg/yr.
119 Their analysis revealed the spatial heterogeneity in the observed O_2 trends. Significant and extensive
120 O_2 declines were observed in the subpolar North Pacific and off the California coast, while a modest
121 O_2 increase occurred in the mid-subtropical and western tropical North Pacific.

122

For horizontal broad-scale trends in the North Pacific, Stramma et al. [2020] analyzed horizontal data using data from the Hydro base and the World Ocean Database bottle, and found linear trends and the Pacific Decadal Oscillation (PDO) in the tropical and eastern Pacific Ocean, In particular, they found that climate signals such as the North Pacific Gyre Oscillation (NPGO) in the North Pacific, and the 18.6-year oscillation at depths between 50 and 300 m in the equatorial and North Pacific are found, as are physical fields such as water temperature and salinity. Although they collected as much data as possible and analyzed them separately by region, it was difficult to ascertain the physical significance of how these data trends are connected or not. Several historical studies have revealed the existence of O_2 changes with stronger amplitudes and non-uniform local regional patterns in specific areas [Sasano et al. 2015; 2018; Ito et al. 2017; 2024; Stramma et al., 2020; Kolodzijejczyk et al. 2024]. These phenomena should be linked to physical factors such as changes in circulation and stratification, as well as to changes in biological activity that accompany physical changes in dissolved O_2, to some extent.

Opportunities to understand specific trends in dissolved O_2, including those associated with trends in ocean temperature and salinity, are currently limited and will remain so in the future due to constrained observational resources. Data such as those from GOBAI-O_2 will therefore become increasingly valuable for understanding trends at basin scales. Understanding how dissolved O_2 is changing is also crucial for assessing the impact on marine organisms [Breitburg et al. 2018]. Argo floats equipped with oxygen sensors will continue to be deployed in the future. In this study, we present the linear trends of temperature, salinity, and dissolved O_2 using the GOBAI-O_2 data set from 2004 to 2023 in the North Pacific, and how their trends connect to each other. In the discussion section, we show how oxygen changes are influenced by physical factors such as global warming and the physical oceanic circulation in the North Pacific.

2. Data and Methods

The four-dimensional gridded product (GOBAI-O_2) data on ocean interior oxygen are generated using machine learning algorithms trained on dissolved O_2 data from Argo float sensors and ship-based discrete observations. These data are applied to temperature and salinity distributions constructed from the global Argo array [Roemmich and Gilson, 2009]. The GOBAI-O_2 data originate from the combined datasets of ship-based surveys (GLODAP version 2022) and Argo float data (Argo Global Data Assembly Centres), which are processed after quality control [Sharp et al., 2023] (https://doi.org/10.25921/z72m-yz67). The combined dataset served as training input for machine learning algorithms to predict dissolved O_2 [O_2], based on variables such as absolute salinity, conservative temperature, potential density anomaly, hydrostatic pressure, bottom depth, and additional spatiotemporal information representing geographic, seasonal, and interannual variability. While biological processes are not directly incorporated into the machine learning algorithms, Giglio et al. [2018] showed how incorporating spatiotemporal variables can effectively capture their influence implicitly for biological processes.

The development of GOBAI-O_2 involved the use of these two types of machine learning algorithms—random forest regressions and feed-forward neural networks: feed-forward neural networks (FNNs) and random forest regressions (RFRs) [Breiman, 2001]. The average of the FNN and RFR estimates was used as the [O_2] estimate for a given input data point. The data cover 86% of the global ocean area on a 1° × 1° (latitude × longitude) grid, spanning the years 2004–2023 with a monthly resolution. The vertical levels range from the ocean surface to a depth of 2 km, with 58 levels. Sharp et al. [2023] evaluated 0.79 ± 0.04% per decade decrease in the oxygen inventory of the upper 2 km of the global ocean over the period 2004–2022. More details of their data sources, processing, algorithm training, evaluation, and uncertainty estimation are provided in Sharp et al. [2023].

The uncertainty of GOBAI-O_2 datasets [Sharp et al., 2023] is estimated by uncertainty estimates, in which the individual uncertainty components are combined in quadrature (assuming independence) to assess the uncertainty of dissolved O_2 data for each gridded [O_2] value:

$$u([O_2])_{tot.} = \sqrt{u([O_2])^2{}_{meas.} + u([O_2])^2{}_{grid.} + u([O_2])^2{}_{alg.}} \quad (1),$$

where $u([O_2])^2{}_{meas.}$ represents the measurement uncertainty of the $[O_2]$ observation themselves, $u([O_2])^2{}_{grid.}$) reflects the gridding uncertainty arising from a single $[O_2]$ value to represent a four-dimensional box that is coarser in time and space than the resolution of many processes influencing $[O_2]$, and $u([O_2])^2{}_{alg.}$ corresponds to the algorithmic uncertainty from the machine-learning methods used to estimate $[O_2]$ on the grid of Roemmich and Gilson (2009) data. We use this uncertainty estimate $u([O_2])_{tot.}$ and evaluate their uncertainty for estimating oxygen trends (Figs. 1–4). The mean uncertainty is added when calculating the linear trend in oxygen for almost all figures in this study.

The GOBAI-O_2 data are the oxygen data on 1° × 1° horizontal grid with 58 vertical levels at the following depths: 2.5, 10, 30, 40, 50, 60, 70, 80, 90, 100, 110, 120, 130, 140, 150, 160, 170, 182.5, 200, 220, 240, 260, 280, 300, 320, 340, 360, 380, 400, 420, 440, 462.5, 500, 550, 600, 650, 700, 750, 800, 850, 900, 950, 1000, 1050, 1100, 1150, 1200, 1250, 1300, 1350, 1412.5, 1500, 1600, 1700, 1800, 1900 and 1975 m). High vertical resolution near the surface is essential for accurately capturing strong temperature, salinity, density, and oxygen gradients in the mixed layer [Kara et al., 2000]. In our analysis relating to the isopycnal surfaces, we interpolated the original GOBAI-O_2 data to 1-m vertical resolution using cubic spline interpolation and gridded them onto a 1° × 1° × 1 m grid, because interpolation makes us evaluate linear trends in potential temperature, salinity, and dissolved O_2 for each latitudinal band at 1° intervals in latitude and at 0.1σ_θ intervals (Figs. 4–7). To evaluate whether

196 this interpolation procedure is appropriate or not, we also conducted sensitivity tests using multiple
197 interpolation methods (linear, shape-preserving cubic (PCHIP)) and coarser vertical grids (2m and 5m).
198 The results showed no clear differences among the three interpolation methods (Figures S1 (a, b) and
199 S2 (a, b)). A 5-m grid fails to resolve densities lighter than 24.0σ_θ at some latitudes, but we confirmed
200 that the main features of the fields are preserved across all tested resolutions.

201

202 In Section 3.3.2, we have utilized the model outputs from the eddy-resolving OGCM for the Earth
203 Simulator (OFES) [Masumoto et al., 2004; 2010; Sasaki et al., 2008] to examine a relevant physical
204 process. The OFES model is based on the Modular Ocean Model (MOM3) [Pacanowski and Griffies,
205 2000]. The quasi-global configuration of the OFES covers 75° S– 75°N with a horizontal resolution
206 of 0.1° x 0.1°and 54 vertical levels. The model is initialized from a state of rest using the World Ocean
207 Atlas 1998 (WOA98) [Boyer and Levitus, 1997], and spun up for 50 years with the climatological
208 forcing data of the National Centers for Environmental Prediction/National Center for Atmospheric
209 Research (NCEP-NCAR) reanalysis [Kalnay et al., 1996]. After the 50-year spin-up, a hindcast
210 experiment is conducted from 1950 to 2024 using daily atmospheric forcing from the NCEP-NCAR
211 reanalysis. In this study, we used the OFES data from 1950 to 2023.

212

213 ## 3. Results

214 ### 3.1 Horizontal distributions of linear trends

215 Figure 1 shows the horizontal and vertical distributions of linear trends in potential temperature,
216 salinity, dissolved O_2, from 2004 to 2024. Positive trends in potential temperature are primarily
217 distributed in the surface layer above 200 m depth (Fig. 1a–c). Trends are relatively strong in the higher
218 latitudes. Negative trends appeared below the surface from the eastern tropical area (180°–120°W, 5°–
219 15°N) (Fig. 1b). This area extends westward and deepens with increasing depth (Fig. 1d–f). Positive

and negative trends are distributed differently in the subarctic and subtropical gyres below 400 m depth.

Negative trends in salinity are generally observed throughout the surface layer (Fig. 1h–i), with localized positive trends in the Kuroshio–Oyashio transition area and the northwest Pacific (140°–180°E, 20°–50°N), as well as in the tropical region (120°–170°E, 0°–10°N). Some positive trends are also detected in the eastern California coastal area (130°–199°W, 20°–40°N). Below 200 m depth, weak positive and negative trends are evident, mirroring the trends in potential temperature (Fig. 1j–k). Positive and negative trends tend to be distributed differently in the subarctic and subtropical gyres. The negative trends are detected around the Alaska gyre (170°–130°W, 40°–55°N) (Fig. 1j-l), which differs from the distribution of potential temperature.

Negative trends in dissolved O_2 are distributed both horizontally and zonally throughout the depth range (Fig. 1o–u). Large negative trends are observed in the high latitudes and are weaker with latitude near the surface (Fig. 2). The location of these trends shifts with depth. Notably, large negative trends occur along the northeast coastal region (140°–130°W, 40°–50°N) and the southern region (10°–25°N) within the density range of 25.2–26.8σ_θ, from 200 to 600 m depth (Fig. 1q–s). Weak positive trends are partially detected around the Kuroshio–Oyashio transition area (130°–150°E, 30°–40°N) below 200 m depth. These positive trends extend into deeper layers and spread northeastward across the North Pacific (Fig. 1r–u). Positive trends are only observed in specific regions: the tropical region at 100 m depth (Fig. 1p); the Alaska Gyre at 200–400 m depth (Fig. 1q–r); the western tropical region at 400–600 m depth (Fig. 1r–s); and the Kuroshio–Oyashio transition region at 400–600 m depth (Fig. 1r–s). If we see the linear trends in dissolved oxygen by latitude, the magnitudes of the negative latitudes not necessary rely on the latitudes only, because the magnitudes in the surface layer (above 200m depth) is shown in the higher latitude, but in case of the middle depth layer (400–600m), the

magnitude of negative liner trends in the middle latitude (30–40°N) is the largest. This pattern completely implies the remote transports with the circulation. The mechanism of this pattern is discussed more in the later sections (Section 3.3).

The total uncertainty in dissolved O_2, $u([O_2])_{tot.}$, in these layers (Fig. 1v–bb) indicates that large values exist in the northern Pacific above 50°N and gradually become smaller to the south. The relatively large uncertainty values are shown in the surface layer, and the steeper gradients of density in the tropical eastern region [150°–120°W, 10–30°N] at 100–200m depth (Fig. 1w–x). These large uncertainties typically exhibit a maximum of 100 m and tend to decrease with depth (Fig. 2 and Figure A14 in Sharp et al. [2023]). Regionally large uncertainty has been shown to depend primarily on algorithmic uncertainty in Figure 8 in Sharp et al. [2023] among the three components (measurement uncertainty, gridding uncertainty, and algorithm uncertainty) contributing to the total uncertainty (Eq. 1). Algorithmic uncertainty generally decreases with increasing spatio-temporal coverage of the available training data. The fact that greater regional algorithmic uncertainty is observed in the northern Pacific above 50°N and in the western and eastern Pacific coastal regions below 20°N suggests that the sampling data are sparse in those areas, and actually, their data sampling is low (Figure 1 in Sharp et al. 2023).

Compared with the historical horizontal distributions of dissolved O_2 in the North Pacific reported by Ito et al. [2017] (Figure 3 in Ito et al. 2017), our negative trend extends over a broader area. The positive trend detected in the Kuroshio-Oyashio Transition Zone and the northeastern region, with a density range of 26.8–27.0σ_θ (Figure 1r), was not evident in the distribution presented by Ito et al. [2017]. Similarly, the positive trend observed in the tropical western Pacific below 400 m depth (Figure 1r–t) is relatively stronger than that identified in their analysis (Figure 3 in Ito et al. [2017]). The

positive trend in dissolved O_2 in the Kuroshio–Oyashio Transition Zone coincides with a region of low uncertainty values (Fig. 1p–s and 1w–y), suggesting this signal may result from the high observation frequency by Argo profiling floats. Other regions exhibiting positive signals—the northeastern region with a density range of 26.8–27.0σ_θ (170°E–150°W, 45–55°N, Fig. 1r) and the tropical western Pacific (130°–170°E, 0°–10°N, Figure 1r–t)—also correspond to areas of low uncertainty (Fig. 1y-aa). Therefore, these pronounced positive trends likely represent highly reliable increases in dissolved O_2, implying a robust deoxygenation signal.

Some artificially induced or unnatural expansions of the trend are also observed (e.g. 170–130°W, 0–20°N), particularly in dissolved O_2 (Fig. 1q–s; Fig. 4i). The uncertainty estimates (Fig. 1v-bb) clearly indicate certain locations and depths with large values, sometimes exceeding 15 μmol/kg. Uncertainties are generally within 10 μmol/kg in the North Pacific. Such large uncertainties arise from limited observational data and high background variability [Sharp et al. 2023]. Areas with strong variability and steep background O_2 gradients tend to exhibit larger uncertainties than the global mean. An additional potential source of errors is a bias in sensor calibration for Argo-O_2 observations, which may arise from the finite response time of optode sensors and can cause systematic bias in the oxycline regions [Bittig et al., 2014; 2018a,b]. Despite these uncertainties, our analysis shows that the observed trends are spatially coherent and connected smoothly each other, and then we can relate them to well-known physical mechanisms in the North Pacific. The GOBAI-O_2 dataset is, therefore, expected to provide improved insights into other oceanic biogeochemical processes and physical phenomena from an aerial perspective.

3.2 Vertical sections and isopyncal density analysis of liner trends in 137°E and 165°E lines

We picked up the vertical sections and isopycnal density distributions of linear trends in potential temperature, salinity, and dissolved O_2 along the 137°E and 165°E lines to compare with historical observational results reported by Ogata and Nonaka [2020] and Sasano et al. [2015] (Fig. 3). Ogata and Nonaka [2020] used temperature and salinity data from 40 years of cruises along the 137°E line between 1967 and 2009, while Sasano et al. [2015] analyzed temperature, salinity, and dissolved O_2 data from 25 years of cruises along the 165°E line between 1987 and 2011.) Large negative trends in temperature and salinity were detected along the 25.0–26.0σ_θ isopycnal, corresponding to a potential temperature of 10–12°C and salinity of 34.4–34.5. In contrast, large negative trends in dissolved O_2 were observed along the 26.0–27.0σ_θ isopycnal, indicating that the areas showing significant trends in dissolved O_2 differ from those of temperature and salinity. Additionally, large positive trends in dissolved O_2 were observed south of 15°N below 200 m depth along the 137°E line (Fig. 3c), corresponding to the upper boundary of the OML. Compared with the trends in dissolved O_2 (Fig. 3c, g) and associated uncertainties (Fig. 3d, h), the regions exhibiting positive or negative oxygen trends do not overlap with areas of large uncertainty, which means that such oxygen trends are highly reliable in this dataset.

The distributions of trends in temperature and salinity on the isopycnal surfaces show distinct differences for temperatures, salinity, and dissolved O_2 (Fig. 4). The linear trends in temperature and salinity are closely aligned, indicating that warming occurs with increasing salinity, while cooling occurs with decreasing salinity (Fig. 4a–b, d–e). Distinct positive trends in temperature and salinity are observed in the density range of 22.0–26.0σ_θ in the tropical region (5°S–5°N). No noticeable trends are found in the salinity minimum region (S = 34–34.1) within the density range of 26.5–27.0σ_θ. At higher latitudes (40°–50°N), large positive trends are evident in the density range of 26.0–27.0σ_θ (Fig. 4e). For dissolved O_2, negative trends dominate overall; however, weak positive trends are observed throughout the density range of 23.0–26.0σ_θ in low-latitude regions (5°S–5°N).

316 Additionally, large positive trends are present in the deeper density range of 26.0–27.0σ_θ in the 5°–
317 10°N band. Weak positive trends are also detected between 10°–20°N in the density range of 23.0–
318 25.0σ_θ along both the 137°E and 165°E lines.

319

320 The temperature and salinity of GOBAI-O_2 data [Roemmich and Gilson, 2009; Sharp et al., 2023]
321 reveal a much wider area with negative trends in salinity in the density range of 22.0–24.0σ_θ along the
322 137°E line compared to the results reported by Ogata and Nonaka [2020], who examined the OFES
323 data. The general characteristics of the linear trends in potential temperature and salinity align closely
324 with the findings of Sasano et al. [2015], although the current results are notably smoother,
325 particularly for dissolved oxygen. This smooth distribution may be due in large part to the smoothing
326 process applied to the data. The shipboard observations by Sasano et al. [2015] identified patchy
327 positive trends in oxygen within the density range of 24.5–27.5σ_θ in the regions of 5°–15°N and 6°S–
328 1°N. In contrast, the current data depicts a broader, smoother, and more consistent positive trend
329 spreading in the tropical region (-6°S–5°N). The repeated shipboard observations also identified
330 localized positive trends in deeper layers within the density range of 26.5–27.5σ_θ. However, the current
331 data more clearly highlights the core of negative trends in oxygen within 5°–15°N (Fig. 3c and f).
332 These trends represent the negative signals extending along the lower isopycnals, which are
333 characteristic of the subtropical gyre.

334

335 **3.3 Horizontal distribution of linear trends along isopycnal surfaces**

336 **3.3.1 Potential temperature and salinity**

337 The horizontal distributions of linear trends in potential temperature, salinity, and dissolved oxygen on
338 specific isopycnal surfaces at 25.0, 26.0, and 26.8σ_θ (Fig. 5) are illustrated to explore how these trends
339 occur and connect each other. These density surfaces correspond to the shallower densities of

340 Subtropical Mode Water (STMW), the shallower densities of Central Mode Water (CMW) [Suga
341 et al., 1997; 2004], and the representative density of North Pacific Intermediate Water (NPIW)
342 [Nakamura et al., 2000a, b; Nakamura and Awaji, 2003; Yasuda, 2004], respectively. STMW is
343 formed south of the Kuroshio Extension, between 30–35°N and 130–170°E, and penetrates to depths
344 of about 400 m in late winter. It then spreads nearly to the subtropical front through advection across
345 the Kuroshio recirculation area. CMW is formed in the transition area of the central North Pacific and
346 spreads eastward along the North Pacific Current before turning southward and westward in the
347 subtropical gyre [Suga et al., 1997; 2004]. In contrast, NPIW does not outcrop during its formation
348 process in the North Pacific. Its origin lies in Okhotsk Sea Mode Water, which is formed through
349 overturning driven by diapycnal upwelling and tidal mixing around the Kuril Islands [Nakamura et
350 al., 2000a, b; Nakamura and Awaji, 2003; You, 2003; Yasuda, 2004] as well as double diffusions in
351 the North Pacific [You, 2003].

352

353 The distributions of linear trends on the 25.0, 26.0, and 26.8σ_θ isopycnal surfaces indicate that positive
354 and negative trends are linked to specific locations. These trends are generally distributed according
355 to the geostrophic streamlines (Fig. 5a–b, d–e, g–h). Although there are exceptions, such as the region
356 showing weak positive (150–175°E, 20–30°N) (Fig. 5a–b), negative trends in temperature and
357 salinity are predominantly observed in the western and central North Pacific on the 25.0 and 26.0σ_θ
358 isopycnal surfaces (Fig. 5a–b, d–e). Conversely, positive trends in temperature and salinity are
359 primarily distributed in the northeastern and/or eastern side of the North Pacific along the geostrophic
360 streamlines (Fig. 5a–b, d–e). These results mean that the waters subducted in the frontal region with
361 reduced temperature and salinity originate primarily in the northeastern North Pacific and are
362 transported south along geostrophic currents (Figs 5a–b, d–e). There are exceptional areas with
363 warmer and saline waters in the northeast North Pacific (170–130°W, 40–60°N). The exceptional
364 waters affect waters that sink near the Alaska gyre and transport outside the subtropical gyre, and along

365 the California coast.

366

367 As for the water in the density range of 26.8σ_θ (Fig. 5g-h), it exhibits large positive trends in potential
368 temperature and salinity along the Kuril Islands and moderate positive trends on the eastern side of the
369 North Pacific, respectively. Water within this density range (26.8σ_θ) is not directly ventilated but is
370 formed through diapycnal mixing processes [Nakamura et al., 2000a, b; Nakamura and Awaji, 2003;
371 You, 2003; Yasuda, 2004] or double diffusion like a salt finger [You, 2003]. Therefore, the positive
372 trends in the North Pacific likely reflect influences from the oxygen change in the upper layer of 26.8σ_θ
373 (Fig. 5d–e and g–h).

374

375 A meridional northward shift of the outcrop line in the North Pacific due to recent climate changes
376 was detected in the analysis of the OFES data [Ogata and Nonaka, 2020]. Similar northward
377 meridional shifts of the front contour lines at 25.0 and 26.0σ_θ are evident in the current data (Fig. 6).
378 These shifts in outcrop densities are therefore attributed to global warming and can explain the
379 observed negative trends, as less saline water from the subarctic region of the North Pacific is
380 subducted and subsequently transported southward via the subtropical circulation. The positive trends
381 in temperature and salinity occurring in the Alaska region [160–130°W, 30–60°N] (Fig. 5a–b and d–
382 e) may also be attributed to the direct influence of global warming. The 26.0σ_θ fronts shift horizontally
383 rather than vertically between 2004 and 2024 (Fig. 6). Therefore, it should be directly affected by the
384 warming and salinity decrease due to global warming, rather than by the water level-directed spreading
385 of the water temperature-salinity distribution.

386

387 **3.3.2 Dissolved oxygen**

388 The linear trends in dissolved oxygen on the isopycnal surfaces at 25.0, 26.0, and 26.8σ_θ exhibit

predominantly negative trends across the North Pacific (Fig. 5c, f, i), but the spatial distributions of these trends are not uniform. Large negative trends are concentrated in the northeastern and eastern regions, gradually decreasing toward the west (Fig. 5q, f, and i). However, there are exceptions, particularly in the tropical regions, with notable positive trends observed in the western tropical areas on the 26.0 and 26.8σ_θ isopycnal surfaces.

The change of dissolved O_2 was decomposed with the same method of Sasano et al. [2015]. The processes and derivation underlying the equations (Eqs. 2, 3) for the change of dissolved oxygen are as follows. We tried to calculate each factor below and discussed the contributing factors for the dissolved oxygen.

$$\frac{\partial O_2}{\partial t} = \left(\frac{\partial O_2}{\partial z}\frac{\partial z}{\partial t}\right) + \left(\frac{\partial O_2^{sat}}{\partial t}\right)_{net} - \left(\frac{\partial (AOU)}{\partial t}\right)_{net}, \quad (2)$$

and consequently, they proposed the following equation:

$$\frac{\partial O_2}{\partial t} = \left(\frac{\partial O_2}{\partial z}\frac{\partial z}{\partial t}\right) + \left(\frac{\partial O_2^{sat}}{\partial t} - \frac{\partial O_2^{sat}}{\partial z}\frac{\partial z}{\partial t}\right) + \left(-\frac{\partial (AOU)}{\partial t} + \frac{\partial (AOU)}{\partial z}\frac{\partial z}{\partial t}\right). \quad (3)$$

(i) (ii) (iii) (iv) (v) (vi)

$\partial O_2/\partial t$ ($X = O_2$, O_2^{sat}, AOU (Apparent Oxygen Utilization)) and $\partial z/\partial t$ denote the temporal rate of change in the depth of the isopycanl horizon (z), while $\partial X/\partial z$ indicates the vertical gradient of the variable X at that horizon., The latter was averaged over the past 20 years in this analysis. The term ($\partial X/\partial t$)$_{net}$ represents the net change in a variable X. By applying Eq. (3) to the time-series data of the reconstructed O_2 data estimated from the linear regression analysis, the rate of O_2 change on each isopycnal surface (i) was attributed to various factors: (ii) the apparent effect of the deepening of isopycnal surface due to warming/freshening; (iii) the effect of O_2^{sat} change due to temperature/salinity changes; (iv) the effect of the deepening/shallowness of isopycnal surfaces with temperature/salinity changes; (v) the changes in AOU resulting from factors such as disequilibrium

412 with atmosphere, biological activities with lateral advection and/or circulation (the elapsed time after
413 the water lost contact with the atmosphere); (vi) the effect of deepening/shallowing of AOU changes
414 unrelated to O_2^{sat}. (The schematic illustrating the decomposition of oxygen change following
415 equations (2, 3) is shown in Supplementary Figure S5 after Sasano et al. [2015].)

416

417 Figure 7 shows the horizontal distributions of the magnitude of each factor contributing to the rate of
418 O_2 change on $25.0\sigma_\theta$, $26.0\sigma_\theta$, and $26.8\sigma_\theta$ surfaces. The results showed that the prominent O_2 declines
419 (Fig. 5c, f, i) are driven by multiple contributing negative and positive factors. The dominant factors
420 vary by latitude. Around the Alaska Gyre in higher latitudes (170–130°W, 40–60°N), the primary
421 contributors to O_2 decline are the deepening of isopycnal surfaces (ii) and the shallowing of AOU
422 changes (vi) (Fig. 7f, j, k, o). The effect of O_2^{sat} change due to temperature/salinity (iii) and the AOU
423 changes (v) are affected oppositely at that time. The negative trends in the Bering Sea (150°E–170°W,
424 50–60°N) (Figs. 5o) can be judged to be mainly affected by the AOU changes (v) (Fig. 7n).

425

426 In contrast, the O_2 decline in the subtropical and mid-latitudes (10–40°N) is largely driven by AOU
427 changes (v) (Fig. 7d, i, and n). The relative weakening of the total O_2 decline in the western North
428 Pacific (Fig. 5c, f, i) is influenced by positive O_2 changes (Fig. 7f and k). Such positive trends are
429 driven by O_2^{sat} changes due to temperature and salinity (Fig. 7b), and the vertical movement of AOU
430 changes (Fig. 7j and o, Fig. 8b–c).

431

432 Slightly in the mid-ocean between 170°E and 160°W, the positive trend pattern shows a negative trend,
433 but in the North Pacific Ocean between 30°N and 50°N, there is a pronounced positive trend

434 continuously extending from east to west (Fig. 7i and n). This phenomenon may be related to the
435 northward meridional shift of the fronts between the subtropical and subarctic regions due to global
436 warming [Ogata and Nonaka, 2020]. With deeper winter convection, more nutrients are introduced
437 into the surface layer, potentially enhancing biological activity and leading to an increase in AOU.
438 One area of NPIW formation near the Kuril Islands exhibits negative trends in factor (iii) (Fig. 7l).
439 This result suggests weaker vertical mixing during the observational period, likely related to enhanced
440 surface-layer stratification. Supporting this, the current data show positive trends in both temperature
441 and salinity in this region (Fig. 5g–h).

442

443 The increases in dissolved O_2 are particularly prominent in the western tropical area at the density
444 range of 26.8–27.2 σ_θ (Fig. 3c and g; Fig. 4c and g; Fig. 5c, f, and i). This area overlaps with the
445 OML [Reid, 1997]. A similar tendency has also been reported by Sasano et al. [2015] and Takatani
446 et al. [2012]. In this area, the physical variability of the North Equatorial Counter Current (NECC)
447 is likely relevant. Following Chen et al. [2016], the NECC exhibits two distinct modes of variability –
448 interannual and interdecadal– based on the outputs of a multidecadal (1960–2014) ocean general
449 circulation model for the Earth Simulator (OFES). The first mode fluctuates on an interannual
450 timescale, strengthening with a southward migration. The second mode occurs on an interdecadal
451 timescale and is characterized by a progressive weakening in strength, poleward migration, and
452 broadening in width. Their analysis further suggested that, for the second mode, a decrease in wind-
453 curl intensity near the equator was responsible for the weakening, poleward migration, and widening
454 of the current.

455

456 The time-varying signals in the western tropical Pacific in the OFES data are validated by Chen et al.
457 [2016]. We then examined the OFES data (1950–2023), as well, for poleward, eastward velocities,
458 as well as potential temperature and salinity here. The potential temperature anomalies in the OFES
459 data (Fig. 9c, g) indicate that positive anomalies in 0°–5 °N occur above 250 m depth, whereas negative
460 anomalies appear along the potential density along 26.0σ_θ between 5°–20°N. A similar pattern is also
461 shown in the GOBAI-O_2 data (Fig. 3a). There is a discrepancy: Negative trends in salinity along 26.0σ_θ
462 are captured in GOBAI-O_2 data (Fig. 3 b), whereas positive trends in salinity along 26.0σ_θ are detected
463 in the OFES model (Figs. 9b, f). This discrepancy is likely due to the higher salinity present between
464 200–600 m depth in 0–7°N in OFES, which differs from GOBAI-O_2 data (Fig. 10b, d).

465

466 Anomalies of the poleward and eastward velocities from 1950 to 2023 and from 2024 to 2023 (Fig.
467 9a–b, e–f) indicate that poleward velocities increase around 5°N above 200m depth, while eastward
468 velocities decrease in 0–4°N and increase in 5–7°N. The main axis of eastward velocity certainly shifts
469 poleward in 137 °E lines (Fig. 11a), consistent with changes in the second mode variablity of the
470 NECC detected by Chen et al. [2016]. The maximum of the poleward velocity of the NECC is also
471 shifted northward from 1964 to 2023 continuously (Fig. 11b). The broadening of NECC width was not
472 apparent in this analysis, differing from Chen et al. [2016]. This could be because we analyzed the
473 original data rather than isolating the second EOF mode of the velocities. Examination of the wind-
474 curl intensity in the equatorial region from 1950 to 2023 confirmed that the decreases in wind-curl
475 intensity along the 0°–10°N band and the poleward broadening of the negative wind stress curl have
476 persisted to 2023 (Fig. 12).

477

The westward penetration of the OML is slow, occurring between two eastward-extending tongues of high O_2 water originating from the western boundary around the equator area [Reid, 1997]. The O_2 increase at the density range of 26.8–27.2 σ_θ (Fig. 3c, g and Fig. 4c, g) could therefore be explained from weakening and north-poleward shifts of the second mode of the NECC with interdecadal variability. The O_2 increase (Fig. 1o-u) follows with such physical backgrounds, penetrating larger dissolved O_2 from westward. The depth of the isopycnal surface becomes shallower along the equator during the observational period in the boundary between the subtropical gyre and the tropical region, meaning the boundary shifts to the north along 137°E line.

4. Conclusion

The oxygen variabilities in the North Pacific include the influences of global warming and climate variabilities. This study utilizes the four-dimensional gridded [O_2] product [GOBAI-O_2] created using artificial intelligence technology [Sharp et al. 2023] based on past potential temperature, salinity, and dissolved O_2 and profiling float data to examine linear trends in temperature, salinity, and dissolved O_2 over the past 20 years (2004–2023) in the North Pacific and the underlying mechanisms. The linear trends in potential temperature, salinity, and dissolved O_2 are consistent with findings from previous studies [Takatani et al. 2012; Sasano et al. 2015; Ogata and Nonaka, 2020], and we explained how they change spatially along 137°E and 165°E (Figs. 3 and 4).

A major achievement of this study is that the GOBAI-O_2 data, being globally gridded, allowed us to show that the trends are smoothly connected, spreading horizontally and vertically to the west and east, presenting a reasonably reliable picture. The horizontal trend mapping over the North Pacific area along the isopycnals was also clarified (Fig. 5). Notably, for the oxygen data, which has fewer observation and a more fragment understanding compared to potential temperature and salinity, we

observed an overall decreasing trend in oxygen. However, in some areas, we also identified locally increasing oxygen trends associated with warming and the northward meridional shift of subtropical and subpolar fronts (Fig. 4). The increasing oxygen trends in the western equatorial region were explained to be linked to the weakening of the second mode of the NECC variability. The decomposition analysis of dissolved O_2 evaluated possible origins of oxygen trends at each isopycnal surface (Fig. 7).

Of course, we need to keep in mind that these datasets are estimated from the available information in temperature and salinity data, and available oxygen data using machine learning methods. So, caution is warranted regarding the results. Future work should compare and validate these results against various reanalysis datasets and other sources. Ito et al. [2024] created a similar O_2 dataset by combining historical shipboard (bottle and CTD-O_2) profiles from 1965 to 2020 and biogeochemical Argo profiles after 2005 using different machine learning approaches, as with the GOBAI-O_2 dataset. Cross-comparisons between their dataset and ours are expected to be beneficial.

The monthly mean climatological GOBAI-O_2 data set should include the Pacific Decadal Oscillation (PDO; Stramma et al., 2020; Pozo Buil and Di Lorenzo, 2017) and the North Pacific Gyre Oscillation (NPGO; Stramma et al., 2020). This dataset is expected to provide a valuable basis for investigating how such climate variation influences dissolved O2 through physical driving mechanisms. These challenges remain topics for future research.

Data availability:

GOBAI-O_2 data is available at https://www.ncei.noaa.gov/access/metadata/landing-page/bin/iso?id=gov.noaa.nodc:0259304. Temperature and salinity are from Roemmich and Gilson

(2009) Argo climatology (https://sio-argo.ucsd.edu/RG_Climatology.html). The OFES and NCEP-NCAR data used in our study are obtained from APDRC, University of Hawaii (http://apdrc.soest.hawaii.edu).

Acknowledgements:

This work was supported by the Institute for Basic Science (IBS), Republic of Korea, under IBS-R028-D1. Jonathan D. Sharp and the reviewers are acknowledged for providing comments that prompted significant improvements to this manuscript.

Author contributions:

MI designed the study, and wrote the initial manuscript draft, and produced all figures. All authors contributed to checking and improving the manuscript.

Financial support:

This research has been supported by the Institute for Basic Science (grant no. IBS-R028-D1) and the Japan Society for the Promotion of Science (JSPS) through a Grant-in-Aid for Scientific Research JP22H00176.

Figure captions:

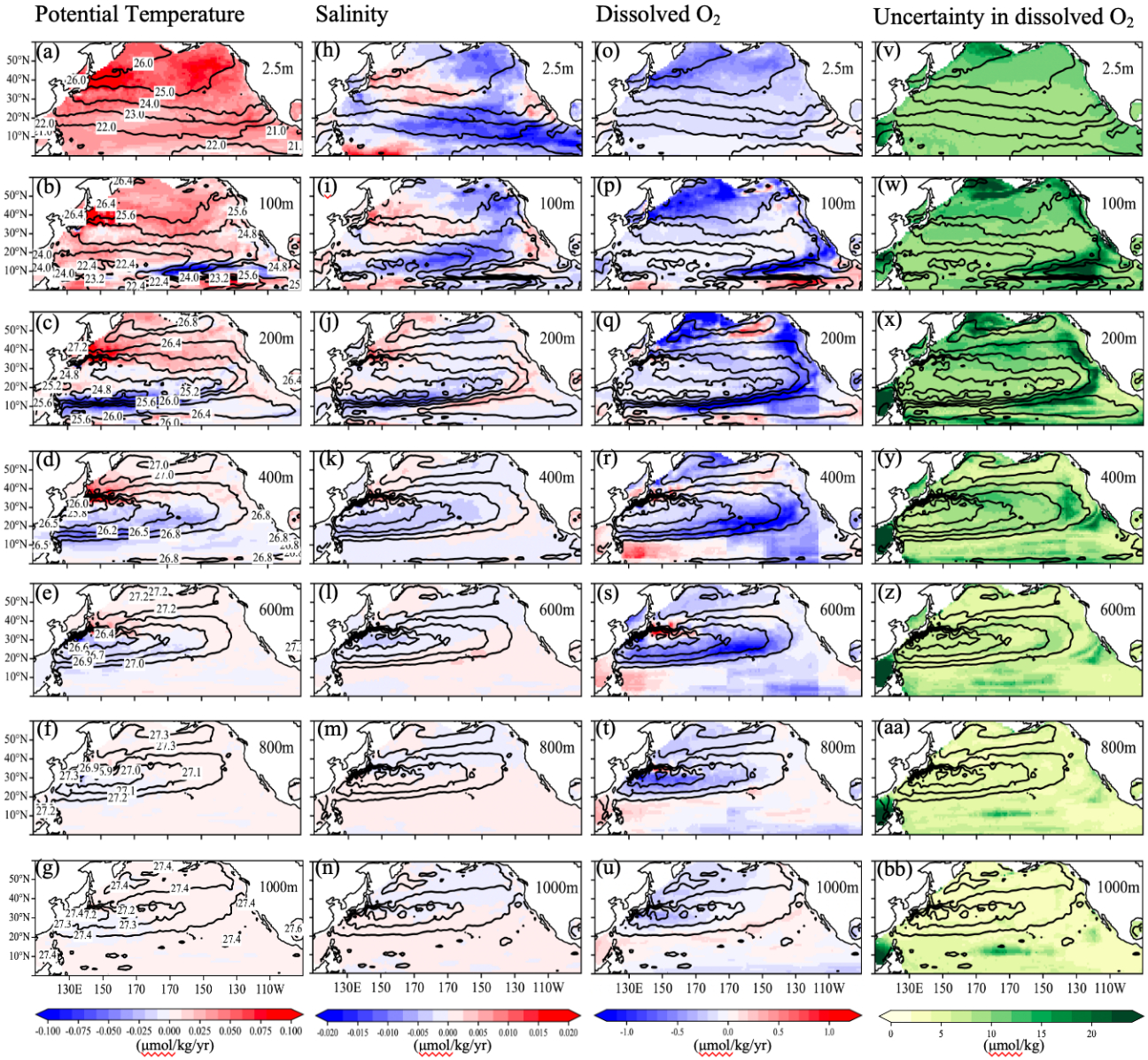

Figure 1 Horizontal distributions of linear trends (μmol/kg/yr) in (a–g) potential temperature, (h–n) salinity, and (o–u) dissolved oxygen (O_2) during the observational period at depths of 0, 100, 200, 400, 600, 800, and 1000 m, respectively. Contours denote potential density at each depth. Labels for the potential density are shown only in the potential temperature sections. Corresponding distributions of the mean uncertainty in dissolved O_2 (μmol/kg) are presented in panels (v–bb).

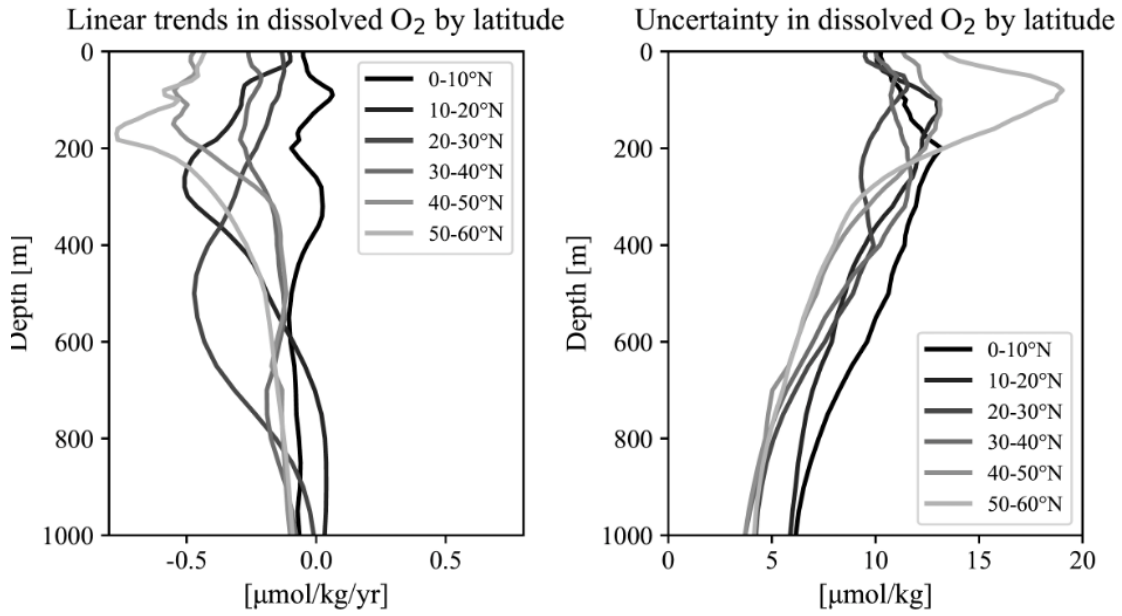

553

554 **Figure 2** Vertical profiles of linear trends and uncertainty in dissolved O_2 by latitude.

555

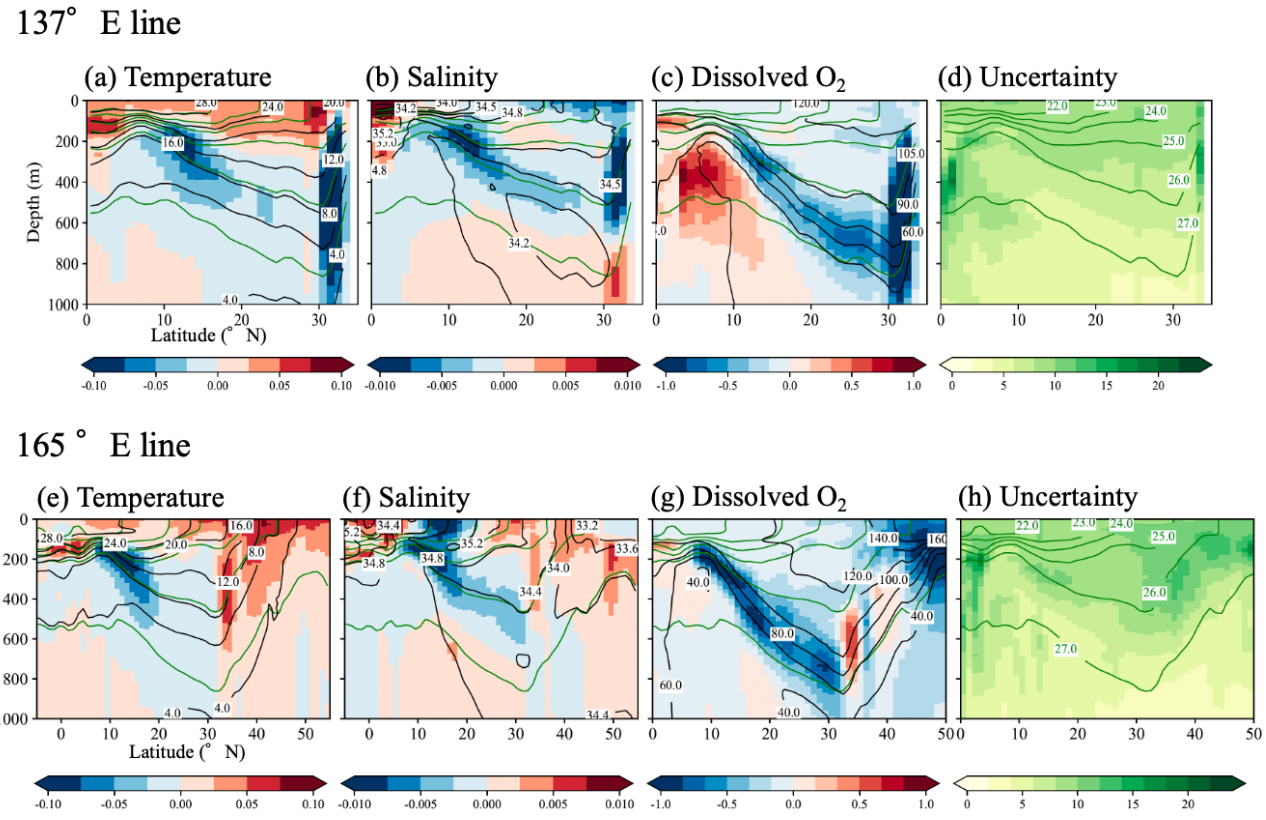

556

557 **Figure 3** Vertical sections showing linear trends in potential temperature (a, e), salinity (b, f), and
558 dissolved O_2 (c, g) along the 137°E and 165°E meridians, respectively. Corresponding vertical sections
559 of the mean uncertainty are presented in panels (d) and (h). Black contour lines indicate the mean

potential temperature (a, e), salinity (b, f), and dissolved oxygen (c, g) over the period 2004–2023, while green contour lines represent the mean potential density. Labels for the potential density are shown only in the uncertainty sections.

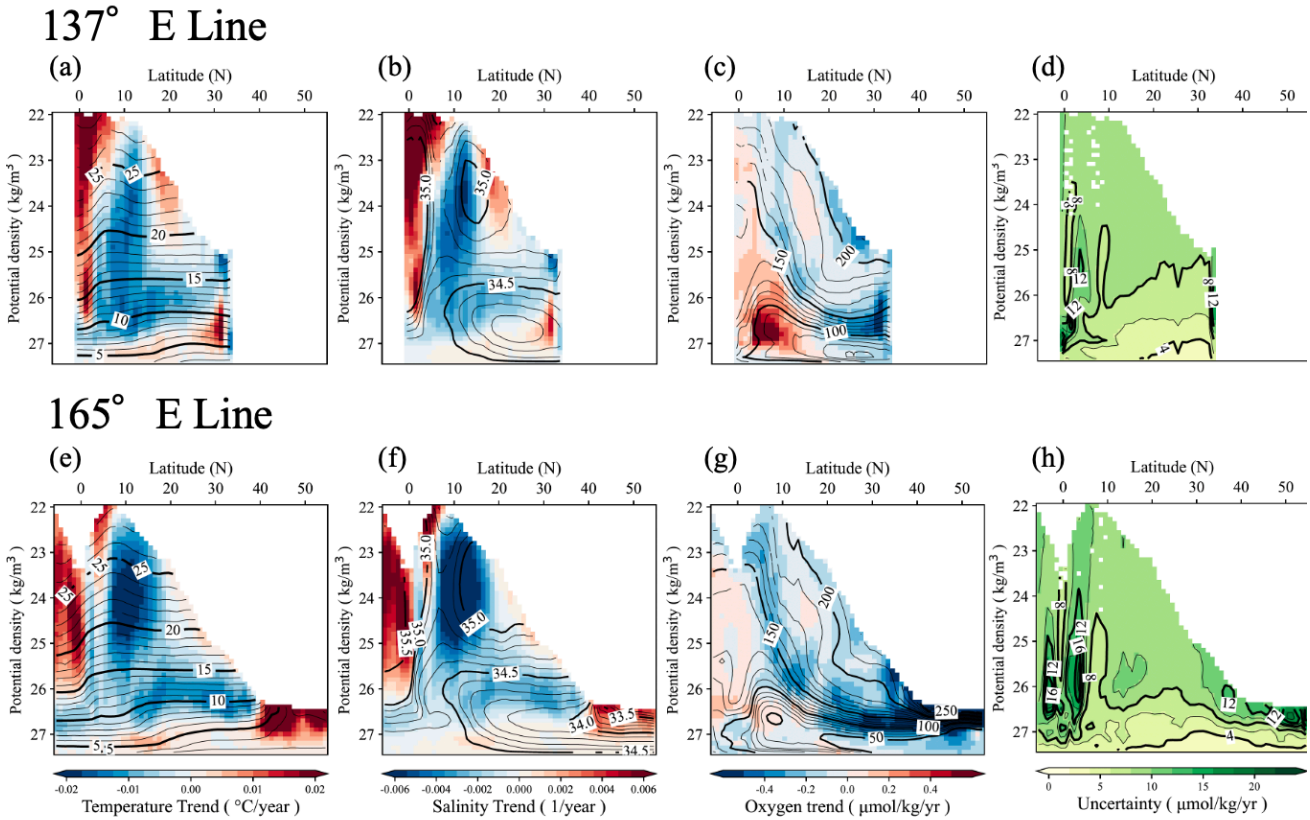

Figure 4 Linear trends in (a, e) potential temperature, (b, f) salinity, (c, g), and dissolved O_2 on each isopycnal surface at intervals of $0.1\sigma_\theta$, calculated at every 1.0 deg of latitude in 137 °E and 165 °E lines, respectively. Contour lines represent the mean values during the target observation periods, plotted at intervals of $0.1\sigma_\theta$ for each 1 deg. of latitude. Fig. 4(d) and 4(h) are the same but show the averaged uncertainty during the target observation periods, on each isopycnal surface.

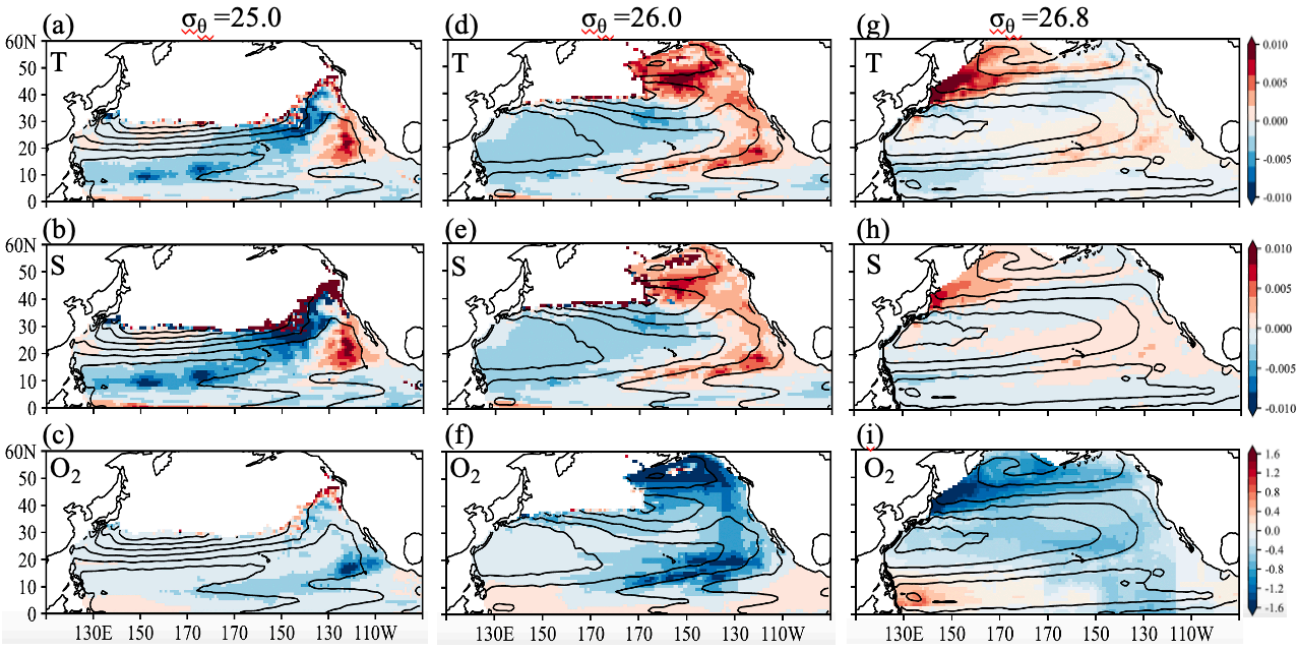

Figure 5 Linear trends in (a) potential temperature, (b) salinity, and (c) dissolved O_2 on each isopycnal surface at 25.0, 26.0, and 26.8σ_θ. Contour lines represent geostrophic flow streamlines on 26.0 and 26.8σ_θ surface, relative to 2000 m.

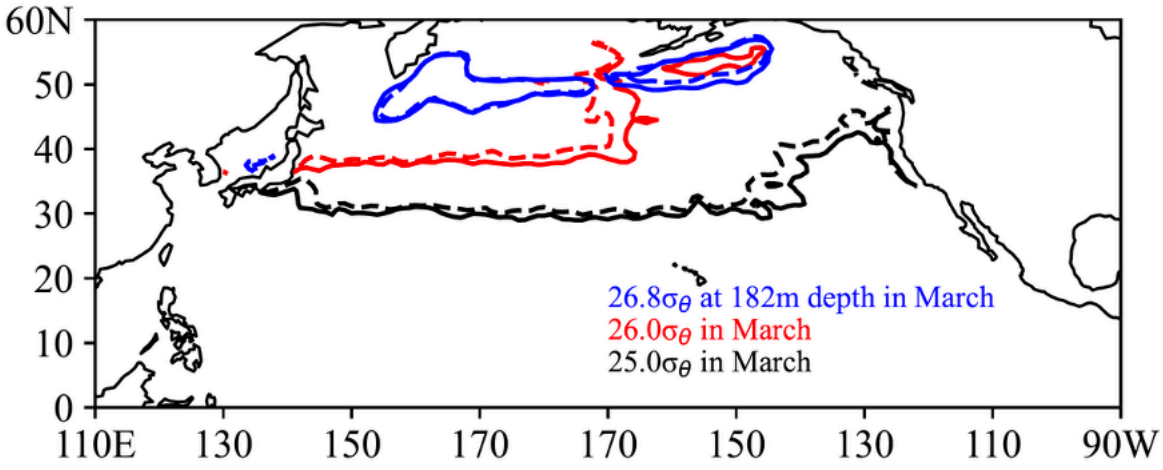

Figure 6 Density contours of 25.0σ_θ (black), 26.0σ_θ (red), and 26.8σ_θ (blue). Solid lines indicate the average density contours for March 2004–2009, while dashed lines represent 2019–2023.

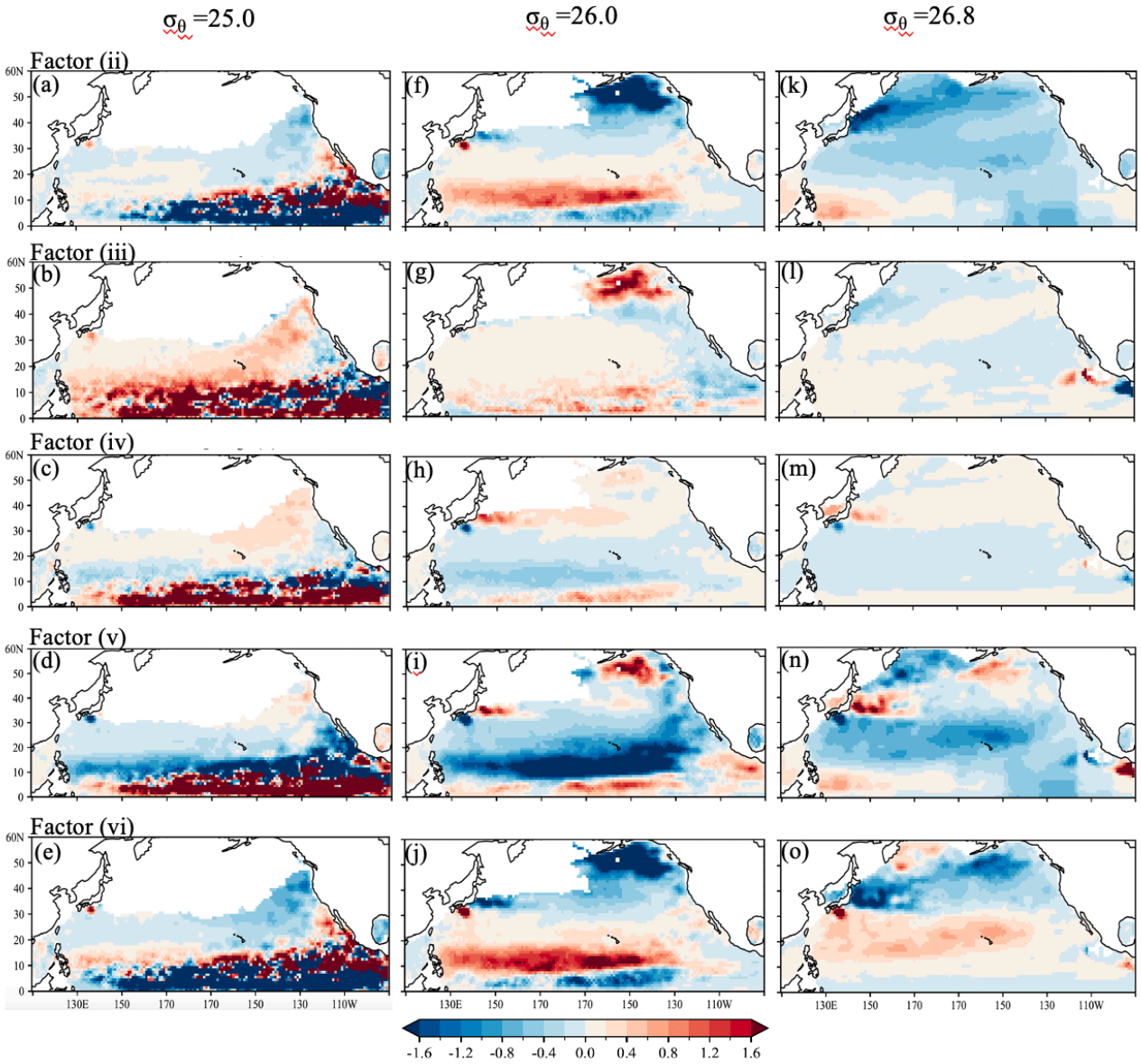

Figure 7 Horizontal distributions of the magnitude of each factor contributing to the rate of O_2 change on 25.0, 26.0, and 26.8 σ_θ in Eq. (1). The rate of O_2 change on each isopycnal surface is attributed to these factors: (ii) the apparent effect of the deepening of the isopycnal surface due to warming/ refreshing, (iii) the effect of O_2^{sat} change due to temperature/salinity changes, (iv) the effect of the deepening/shallowness of isopycnal surfaces with temperature/salinity changes, (v) the changes in AOU resulting from factors such as disequilibrium with atmosphere, biological activities with lateral advection and/or circulation, (vi) the effect of vertical movement (deepening/shallowing) of AOU changes unrelated to O_2^{sat}. This analysis was calculated with the reconstructed O_2 data estimated from the linear regression analysis.

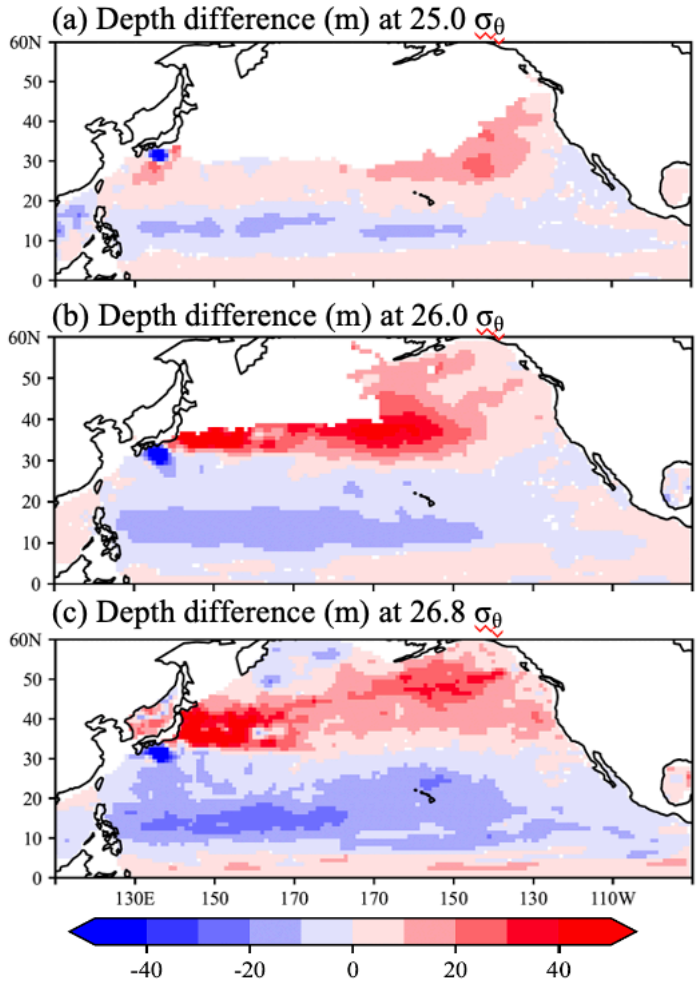

591

592 **Figure 8** Depth difference (m) between the 5-year averaged data in March, 2004–2009 and 2018–2023
593 at 25.0, 26.0, and 26.8σ_θ. The reconstructed O_2 data estimated from the linear regression analysis were
594 used in this calculation. Positive and negative values indicate the deepening and shallowing,
595 respectively, from the depth of each density in 2018– 2023.

596

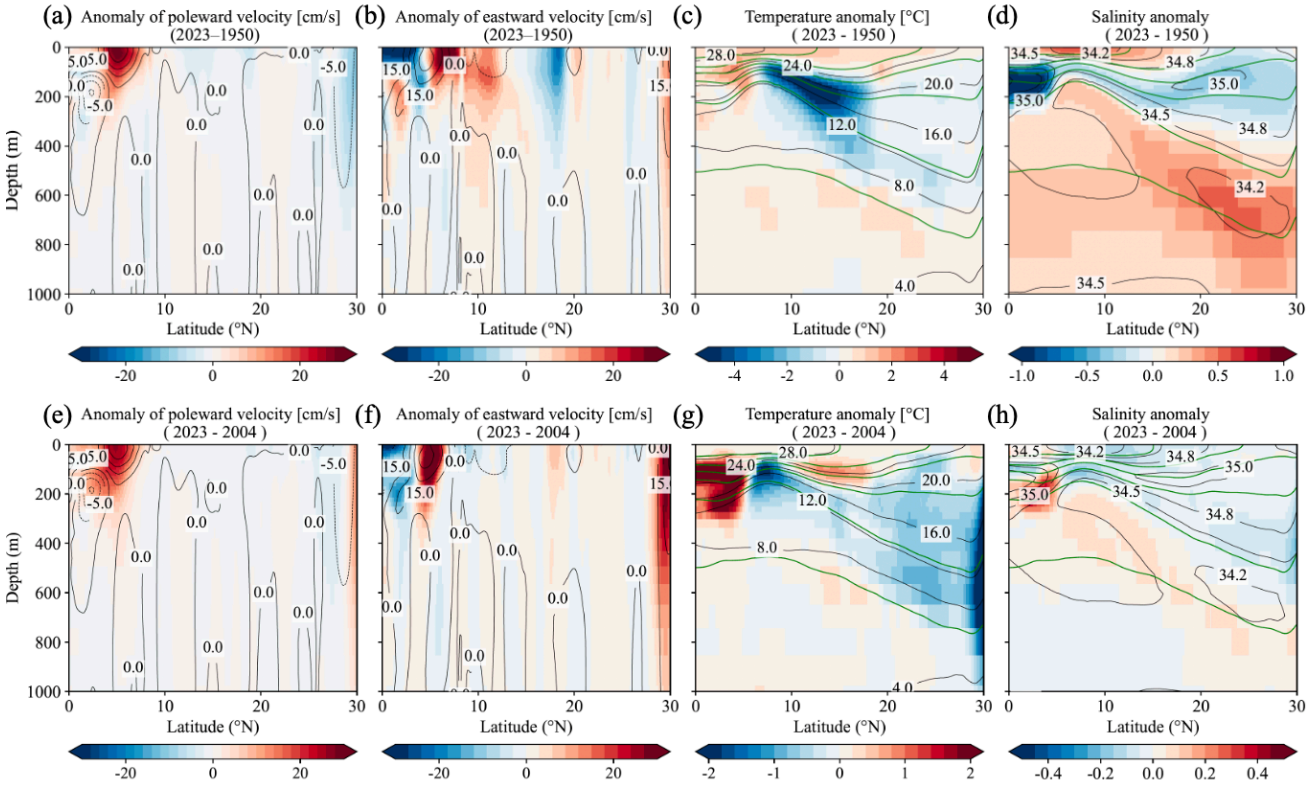

Figure 9. Anomaly of poleward and eastward velocity, potential temperature, and salinity in the OFES model outputs from 1950 to 2023 (a–d) and from 2004 to 2023 (e–h), respectively, in the 137°E line. Contours of averaged values of poleward and eastward velocity, potential temperature, and salinity during the target period are also shown in each figure. Green contour lines in (c–d, g–h) indicate the average potential density of 22, 23, 24, 25, 26, and 27σ_θ, during the target periods.

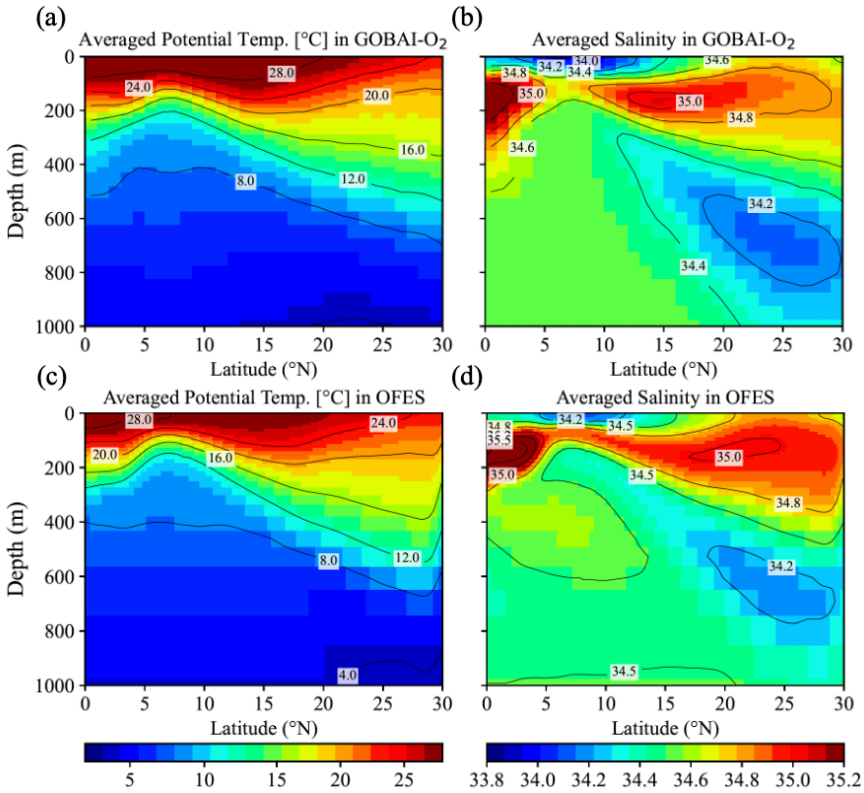

603

604 **Figure 10.** Averaged Potential Temperature (a, c) and salinity (b, d) in GOBAI-O_2 from 2004 to 2023
605 and OFES data from 1950 to 2023, respectively, in the 137°E line.

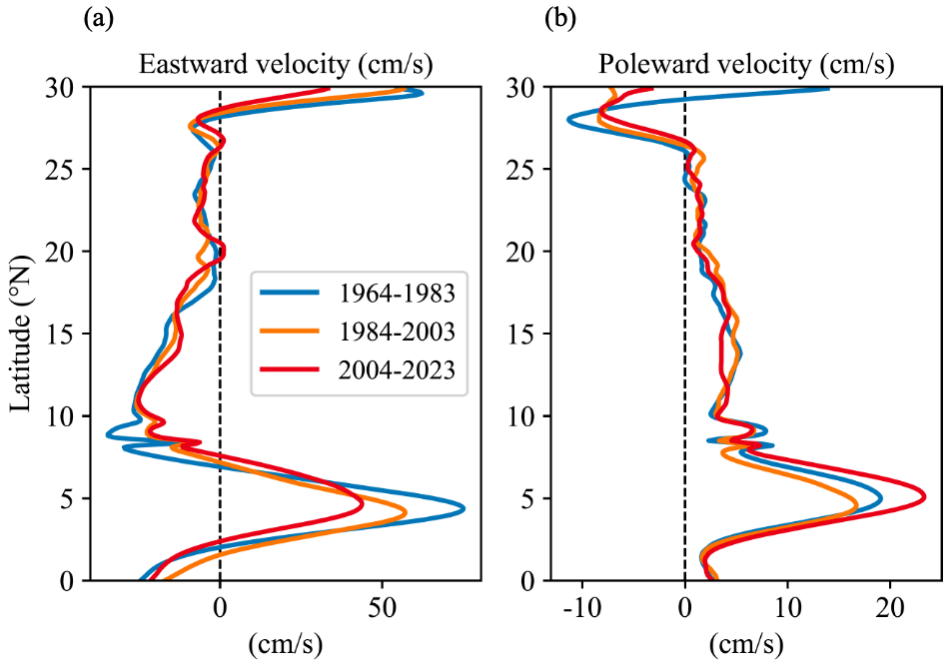

606

607 **Figure 11.** Latitudinal distribution of averaged eastward (a) and poleward velocity (b) in the OFES
608 data from 1964 to 1983, from 1984 to 2003, and from 2004 to 2023, respectively, in the 137°E line.

609

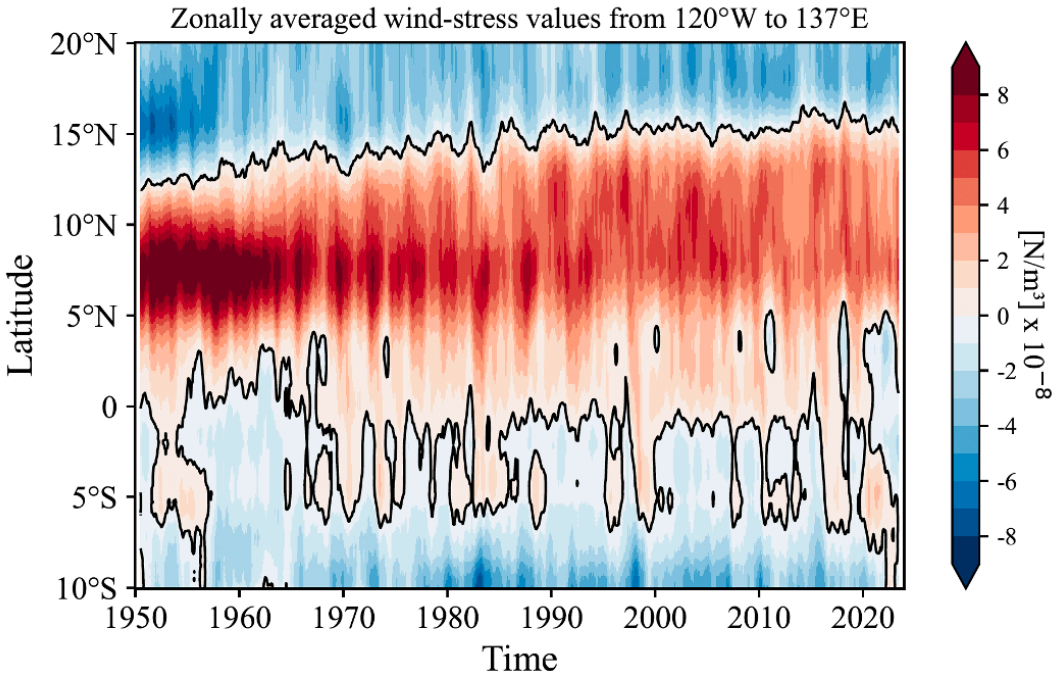

Figure 12. NCEP-NCAR wind-stress curl values zonally averaged from 137°E to 120° W from 1950 to 2023. A 13-month running-mean filter has been applied in time.

Appendix: Essential concepts and derivations for Equation (2-3)

The essential concepts and derivation for equations (2) and (3) were originally proposed by Takatani et al. [2012] and described in detail by Sasano et al. [2015]. We follow their derivation here.

When the temperature at a depth z_A increases from θ_A to θ_A' as a consequence of ocean heat content increase, the density at that depth decreases from σ_A to σ_A'. For simplicity, the vertical profile of salinity is assumed to remain unchanged with time. As a result, the isopycnal surface of σ_A deepens from z_A to z_B (Figure S5). If surface freshening occurs simultaneously due to a net freshwater input, both the density decreases at z_A (from σ_A to σ_A') and the deepening of the isopycnal (from z_A to z_B) are enhanced. Because density is a function of temperature and salinity ($\sigma = f(\theta, S)$), the density of an isopycnal surface σ_A can be expressed as

$$\sigma_A = f(\theta_A, S_A) \qquad \text{(before warming)} \quad \text{(C1)}$$

$$= f(\theta_B', S_B). \qquad \text{(after warming)} \quad \text{(C2)}$$

Here, S_A and S_B denote salinity at depth z_A and z_B, respectively, and θ_B' represents the temperature at σ_A at z_B after warming. To satisfy (C1) and (C2), z_B is determined. In the region where salinity decreases with depth (e.g., above the salinity minimum layer of NPIW), $S_A > S_B$, and thus $\theta_A > \theta_B'$. This means that the potential temperature on an isopycnal surface effectively decreases as a result of warming, implying that biogeochemical properties on an isopycnal surface are also expected to change.

For a tracer X whose vertical profile with respect to depth does not change with time (e.g., salinity; see Figure S5(c)), the temporal change of X on potential density σ_A is attributed to the apparent change caused by the deepening of the isopycnal surface from z_A to z_B:

$$\frac{\partial X}{\partial t} = \left(\frac{\partial X}{\partial z} \cdot \frac{\partial z}{\partial t}\right) \qquad \text{(C3)}$$

Here, $\partial X/\partial t$ represents the temporal change of X observed on σ_A (gray arrows in Figure S5), z the depth at σ_A, $\partial X/\partial z$ the vertical gradient of X with respect to the depth (assumed to be time-invariant), and $\partial z/\partial t$ the rate of increase in the depth of density σ_A. $\partial X/\partial z \cdot \partial z/\partial t$ denotes the effect of deepening (illustrated as white arrows in Figure S5, corresponding to the difference between the filled square and filled circle).

Alternatively, for a variable Y whose vertical profile evolves with time and warming occurs simultaneously, the temporal change of Y at density σ_A can be expressed as the sum of two components: the temporal change associated with the deepening of the isopycnal surface from z_A to z_B and the net temporal change of Y, $(\partial Y/\partial t)_{net}$ between the time before and after warming:

$$\frac{\partial Y}{\partial t} = \left(\frac{\partial Y}{\partial z} \cdot \frac{\partial z}{\partial t}\right) + \left(\frac{\partial Y}{\partial t}\right)_{net} \qquad \text{(C4)}$$

To evaluate the net change $(\partial Y/\partial z)_{\text{net}}$ (illustrated by the black, blue, or pink arrows of a difference in symbols between filled square and open square in Figure S5), it is necessary to evaluate the contribution of the temporal change of Y due to the deepening of the isopycnal surface and to subtract it from the change of Y observed at density σ_A. For instance, the change of O_2^{sat} in Figure S5(f) is observed as a gray isopycnal surface (white arrow). Therefore, the net change (blue arrow) is obtained as a difference between the observed change and the deepening effect.

The dissolved oxygen concentration O_2 can be expressed as:

$$O_2 = O_2^{sat} - AOU \qquad \text{(C5)}$$

where O_2^{sat} is the oxygen saturation concentration (a function of temperature and salinity) and AOU is "apparent oxygen utilization". AOU represents the oxygen consumed by biological activity since subduction. However, these contributions are typically negligible because AOU ≈ 0 in surface waters.

According to (C4), the temporal change of O_2 at a given density for a fixed station is:

$$\frac{\partial O_2}{\partial t} = \left(\frac{\partial O_2}{\partial z} \cdot \frac{\partial z}{\partial t}\right) + \left(\frac{\partial O_2}{\partial t}\right)_{net}. \qquad \text{(C6)}$$

Similarly,

$$\frac{\partial O_2^{sat}}{\partial t} = \left(\frac{\partial O_2^{sat}}{\partial z} \cdot \frac{\partial z}{\partial t}\right) + \left(\frac{\partial O_2^{sat}}{\partial t}\right)_{net}, \qquad \text{(C7)}$$

and

$$\frac{\partial AOU}{\partial t} = \left(\frac{\partial (AOU)}{\partial z} \cdot \frac{\partial z}{\partial t}\right) + \left(\frac{\partial (AOU)}{\partial t}\right)_{net}. \qquad \text{(C8)}$$

The term $(\partial O_2^{sat}/\partial t)_{\text{net}}$ is directly related to a certain value with respect to warming as O_2^{sat} changes as a function of temperature. If AOU does not change with time, i.e., the change in O_2 concentration is attributed only to the change in O_2^{sat}, $(\partial (AOU)/\partial \text{t})_{net} = 0$ and $\partial (AOU)/\partial t$ follow equation

(C3). On the other hand, if AOU varies with time, $\partial(AOU)/\partial t$ follows equation (C4) and $(\partial(AOU)/\partial \mathrm{t})_{net} \neq 0$, as shown by dashed gray line in Figure S5(g).

Since O_2 is expressed as equation (C5), the net temporal change of O_2 on an isopycnal surface is given by:

$$\left(\frac{\partial O_2}{\partial t}\right)_{net} = \left(\frac{\partial O_2^{sat}}{\partial t}\right)_{net} - \left(\frac{\partial (AOU)}{\partial t}\right)_{net}. \qquad \text{(C9)}$$

According to equations (C6) and (C9), the temporal change of O_2 on an isopycnal surface can be expressed:

$$\left(\frac{\partial O_2}{\partial t}\right) = \left(\frac{\partial O_2}{\partial z} \cdot \frac{\partial z}{\partial t}\right) + \left(\frac{\partial O_2^{sat}}{\partial t}\right)_{net} - \left(\frac{\partial (AOU)}{\partial t}\right)_{net}, \qquad \text{(C10)}$$

as described in equation (1) in the main text. Each term in equation (C10) corresponds to an arrow in Figure S5(e): From left to right, these are represented by the gray arrow, white, blue and pink arrows, respectively. The blue arrow is identical to Figure S5(f), while pink arrow corresponds to Figure S5(g), but with its direction reversed. Finally, substituting equations (C7) and (C8) into (C10) yields (C11) (corresponding to equation (2) in the main text):

$$\frac{\partial O_2}{\partial t} = \left(\frac{\partial O_2}{\partial z}\frac{\partial z}{\partial t}\right) + \left(\frac{\partial O_2^{sat}}{\partial t} - \frac{\partial O_2^{sat}}{\partial z}\frac{\partial z}{\partial t}\right) - \left(\frac{\partial (AOU)}{\partial t} - \frac{\partial (AOU)}{\partial z}\frac{\partial z}{\partial t}\right). \text{(C11)}$$

(i) (ii). (iii). (iv) (v) (vi)

Note: The signs in Eq. 3(v) and (vi) are reversed from those in Equations C11(v) and (vi) for convenience.

Data availability:

GOBAI-O_2 [Sharp et al. 2022; 2023] can be accessed from NOAA's National Centers for Environmental Information at https://accession.nodc.noaa.gov/0259304 (doi: 10.25921/z72m-yz67).

692

693 **References:**

694 Alkire, M. B., D'Asaro, E., Lee, C., Jane Perry, M., Gray, A., Cetinić, I., et al. (2012). Estimates of
695 net community production and export using high-resolution, Lagrangian measurements of O2, NO3−,
696 and POC through the evolution of a spring diatom bloom in the North Atlantic. *Deep Sea Research*
697 *Part I: Oceanographic Research Papers*, *64*, 157–174. https://doi.org/10.1016/j.dsr.2012.01.012

698 Berman-Frank, I., Lundgren, P., & Falkowski, P. (2003). Nitrogen fixation and photosynthetic oxygen
699 evolution in cyanobacteria. *Research in Microbiology*, *154*(3), 157–164.
700 https://doi.org/10.1016/S0923-2508(03)00029-9

701 Bittig, H. C., Fiedler, B., Scholz, R., Krahmann, G., & Körtzinger, A. (2014). Time response of oxygen
702 optodes on profiling platforms and its dependence on flow speed and temperature. *Limnology and*
703 *Oceanography: Methods*, *12*(8), 617–636. https://doi.org/10.4319/lom.2014.12.617

704 Bittig, H. C., & Körtzinger, A. (2015). Tackling Oxygen Optode Drift: Near-Surface and In-Air
705 Oxygen Optode Measurements on a Float Provide an Accurate in Situ Reference.
706 https://doi.org/10.1175/JTECH-D-14-00162.1

707 Bittig, H. C., Körtzinger, A., Neill, C., van Ooijen, E., Plant, J. N., Hahn, J., et al. (2018a). Oxygen
708 Optode Sensors: Principle, Characterization, Calibration, and Application in the Ocean. *Frontiers in*
709 *Marine Science*, *4*. https://doi.org/10.3389/fmars.2017.00429

710 Bittig, H. C., Steinhoff, T., Claustre, H., Fiedler, B., Williams, N. L., Sauzède, R., et al. (2018b). An
711 Alternative to Static Climatologies: Robust Estimation of Open Ocean CO_2 Variables and Nutrient
712 Concentrations From T, S, and O_2 Data Using Bayesian Neural Networks. *Frontiers in Marine*
713 *Science*, *5*. https://doi.org/10.3389/fmars.2018.00328

714 Bopp, L., Resplandy, L., Orr, J. C., Doney, S. C., Dunne, J. P., Gehlen, M., et al. (2013). Multiple
715 stressors of ocean ecosystems in the 21st century: projections with CMIP5 models. *Biogeosciences*,
716 *10*(10), 6225–6245. https://doi.org/10.5194/bg-10-6225-2013
717 Boyer, T. P., and S. Levitus (1997), Objective Analyses of Temperature and Salinity for the World
718 Ocean on a 1/48 Grid, vol. 11, NOAA Atlas NESDIS, Natl. Oceanic and Atmos. Admin., Silver Spring,
719 Md.
720 Boyer, T. P., Antonov, J. I., Baranova, O. K., Coleman, C., Garcia, H. E., Grodsky, A., et al. (2013).
721 World Ocean Database 2013. Retrieved from
722 https://repository.oceanbestpractices.org/handle/11329/357
723 Breiman, L. (2001). Random Forests. *Machine Learning*, *45*(1), 5–32.
724 https://doi.org/10.1023/A:1010933404324
725 Breitburg, D., Levin, L. A., Oschlies, A., Grégoire, M., Chavez, F. P., Conley, D. J., et al. (2018).
726 Declining oxygen in the global ocean and coastal waters. *Science*, *359*(6371), eaam7240.
727 https://doi.org/10.1126/science.aam7240
728 Bushinsky, S. M., Emerson, S. R., Riser, S. C., & Swift, D. D. (2016). Accurate oxygen measurements
729 on modified Argo floats using in situ air calibrations. *Limnology and Oceanography: Methods*, *14*(8),
730 491–505. https://doi.org/10.1002/lom3.10107
731 Chen, X., Qiu, B., Du, Y., Chen, S., & Qi, Y. (2016). Interannual and interdecadal variability of the
732 North Equatorial Countercurrent in the Western Pacific. *Journal of Geophysical Research: Oceans*,
733 *121*(10), 7743–7758. https://doi.org/10.1002/2016JC012190
734 Claustre, H., Johnson, K. S., & Takeshita, Y. (2020). Observing the Global Ocean with
735 Biogeochemical-Argo. *Annual Review of Marine Science*, *12*(Volume 12, 2020), 23–48.
736 https://doi.org/10.1146/annurev-marine-010419-010956
737 D'Asaro, E. A., & McNeil, C. (2013). Calibration and Stability of Oxygen Sensors on Autonomous
738 Floats. https://doi.org/10.1175/JTECH-D-12-00222.1

739 Drucker, R., & Riser, S. C. (2016). In situ phase-domain calibration of oxygen Optodes on profiling
740 floats. *Methods in Oceanography*, *17*, 296–318. https://doi.org/10.1016/j.mio.2016.09.007
741 Estapa, M. L., Feen, M. L., & Breves, E. (2019). Direct Observations of Biological Carbon Export
742 From Profiling Floats in the Subtropical North Atlantic. *Global Biogeochemical Cycles*, *33*(3), 282–
743 300. https://doi.org/10.1029/2018GB006098
744 Giglio, D., Lyubchich, V., & Mazloff, M. R. (2018). Estimating Oxygen in the Southern Ocean Using
745 Argo Temperature and Salinity. *Journal of Geophysical Research: Oceans*, *123*(6), 4280–4297.
746 https://doi.org/10.1029/2017JC013404
747 Helm, K. P., Bindoff, N. L., & Church, J. A. (2011). Observed decreases in oxygen content of the
748 global ocean. *Geophysical Research Letters*, *38*(23). https://doi.org/10.1029/2011GL049513
749 Ito, T., Minobe, S., Long, M. C., & Deutsch, C. (2017). Upper ocean O_2 trends: 1958–2015.
750 *Geophysical Research Letters*, *44*(9), 4214–4223. https://doi.org/10.1002/2017GL073613
751 Ito, T., Cervania, A., Cross, K., Ainchwar, S., & Delawalla, S. (2024). Mapping Dissolved Oxygen
752 Concentrations by Combining Shipboard and Argo Observations Using Machine Learning Algorithms.
753 *Journal of Geophysical Research: Machine Learning and Computation*, *1*(3), e2024JH000272.
754 https://doi.org/10.1029/2024JH000272
755 Johnson, K. S., Plant, J. N., Riser, S. C., & Gilbert, D. (2015). Air Oxygen Calibration of Oxygen
756 Optodes on a Profiling Float Array. https://doi.org/10.1175/JTECH-D-15-0101.1
757 Johnson, K. S., Plant, J. N., Coletti, L. J., Jannasch, H. W., Sakamoto, C. M., Riser, S. C., et al. (2017).
758 Biogeochemical sensor performance in the SOCCOM profiling float array. *Journal of Geophysical*
759 *Research: Oceans*, *122*(8), 6416–6436. https://doi.org/10.1002/2017JC012838
760 Johnson, K. S., & Bif, M. B. (2021). Constraint on net primary productivity of the global ocean by
761 Argo oxygen measurements. *Nature Geoscience*, *14*(10), 769–774. https://doi.org/10.1038/s41561-
762 021-00807-z

763 Kalnay, E., Kanamitsu, M., Kistler, R., Collins, W., Deaven, D., Gandin, L., et al. (1996). The
764 NCEP/NCAR 40-Year Reanalysis Project. Retrieved from
765 https://journals.ametsoc.org/view/journals/bams/77/3/1520-
766 0477_1996_077_0437_tnyrp_2_0_co_2.xml
767 Kara, A. B., Rochford, P. A., & Hurlburt, H. E. (2000). An optimal definition for ocean mixed layer
768 depth. *Journal of Geophysical Research: Oceans*, *105*(C7), 16803–16821.
769 https://doi.org/10.1029/2000JC900072
770 Keeling, R. F., Körtzinger, A., & Gruber, N. (2010). Ocean Deoxygenation in a Warming World.
771 *Annual Review of Marine Science*, *2* (Volume 2, 2010), 199–229.
772 https://doi.org/10.1146/annurev.marine.010908.163855
773 Kolodziejczyk, N., Portela, E., Thierry, V., & Prigent, A. (2024). ISASO2: recent trends and regional
774 patterns of ocean dissolved oxygen change. *Earth System Science Data*, *16*(11), 5191–5206.
775 https://doi.org/10.5194/essd-16-5191-2024
776 Körtzinger, A., Schimanski, J., & Send, U. (2005). High Quality Oxygen Measurements from Profiling
777 Floats: A Promising New Technique. https://doi.org/10.1175/JTECH1701.1
778 Kwiatkowski, L., Torres, O., Bopp, L., Aumont, O., Chamberlain, M., Christian, J. R., et al. (2020).
779 Twenty-first century ocean warming, acidification, deoxygenation, and upper-ocean nutrient and
780 primary production decline from CMIP6 model projections. *Biogeosciences*, *17*(13), 3439–3470.
781 https://doi.org/10.5194/bg-17-3439-2020
782 Lauvset, S. K., Lange, N., Tanhua, T., Bittig, H. C., Olsen, A., Kozyr, A., et al. (2022b).
783 GLODAPv2.2022: the latest version of the global interior ocean biogeochemical data product. *Earth*
784 *System Science Data*, *14*(12), 5543–5572. https://doi.org/10.5194/essd-14-5543-2022
785 Li, C., Huang, Jianping, Ding, L., Liu, X., Yu, H., Huang, Jiping, 2020. Increasing Escape of Oxygen
786 From Oceans Under Climate Change. Geophysical Research Letters 47, e2019GL086345.
787 https://doi.org/10.1029/2019GL086345

788 Limburg, K. E., Breitburg, D., Swaney, D. P., & Jacinto, G. (2020). Ocean Deoxygenation: A Primer.
789 *One Earth*, *2*(1), 24–29. https://doi.org/10.1016/j.oneear.2020.01.001
790 Masumoto, Y., Sasaki, H., Kagimoto, T., Komori, N., Ishida, A., Sasai, Y., et al. (2004). A fifty-year
791 eddy-resolving simulation of the world ocean: Preliminary outcomes of OFES (OGCM for the Earth
792 Simulator). Journal of the Earth Simulator, 1,35–56. https://www.jamstec.
793 go.jp/ceist/j/publication/journal/jes_vol.1/pdf/JES1-3.2-masumoto.pdf
794 Masumoto, Y. (2010). Sharing the results of a high-resolution ocean general circulation model under
795 a multi-discipline framework—a review of OFES activities. *Ocean Dynamics*, *60*(3), 633–652.
796 https://doi.org/10.1007/s10236-010-0297-z
797 Maurer, T. L., Plant, J. N., & Johnson, K. S. (2021). Delayed-Mode Quality Control of Oxygen, Nitrate,
798 and pH Data on SOCCOM Biogeochemical Profiling Floats. *Frontiers in Marine Science*, *8*.
799 https://doi.org/10.3389/fmars.2021.683207
800 Nakamura, T., & Awaji, T. (2004). Tidally induced diapycnal mixing in the Kuril Straits and its role
801 in water transformation and transport: A three-dimensional nonhydrostatic model experiment. *Journal*
802 *of Geophysical Research: Oceans*, *109*(C9). https://doi.org/10.1029/2003JC001850
803 Nakamura, T., Awaji, T., Hatayama, T., Akitomo, K., Takizawa, T., Kono, T., et al. (2000a). The
804 Generation of Large-Amplitude Unsteady Lee Waves by Subinertial K1 Tidal Flow: A Possible
805 Vertical Mixing Mechanism in the Kuril Straits. Retrieved from
806 https://journals.ametsoc.org/view/journals/phoc/30/7/1520-
807 0485_2000_030_1601_tgolau_2.0.co_2.xml
808 Nakamura, T., Awaji, T., Hatayama, T., Akitomo, K., & Takizawa, T. (2000b). Tidal Exchange
809 through the Kuril Straits. Retrieved from https://journals.ametsoc.org/view/journals/phoc/30/7/1520-
810 0485_2000_030_1622_tettks_2.0.co_2.xml
811 Nicholson, D. P., & Feen, M. L. (2017). Air calibration of an oxygen optode on an underwater glider.
812 *Limnology and Oceanography: Methods*, *15*(5), 495–502. https://doi.org/10.1002/lom3.10177

Ogata, T., & Nonaka, M. (2020). Mechanisms of Long-Term Variability and Recent Trend of Salinity Along 137°E. *Journal of Geophysical Research: Oceans*, *125*(2), e2019JC015290. https://doi.org/10.1029/2019JC015290

Pacanowski, R. C., and S. M. Griffies (2000), MOM 3.0 Manual, Technical Report 4, 680 pp., Geophys. Fluid Dyn. Lab., Princeton, N. J. Philander, S. G. H. (1990), El Niño, La Niiña, and the Southern Oscillation, pp. 293, Academic Press, San Diego, Calif.

Pörtner, H. O., & Farrell, A. P. (2008). Physiology and Climate Change. *Science*, *322*(5902), 690–692. https://doi.org/10.1126/science.1163156

Pozo Buil, M., & Di Lorenzo, E. (2017). Decadal dynamics and predictability of oxygen and subsurface tracers in the California Current System. *Geophysical Research Letters*, *44*(9), 4204–4213. https://doi.org/10.1002/2017GL072931

Reid, J. L. (1997). On the total geostrophic circulation of the pacific ocean: flow patterns, tracers, and transports. *Progress in Oceanography*, *39*(4), 263–352. https://doi.org/10.1016/S0079-6611(97)00012-8

Roemmich, D., & Gilson, J. (2009). The 2004–2008 mean and annual cycle of temperature, salinity, and steric height in the global ocean from the Argo Program. *Progress in Oceanography*, *82*(2), 81–100. https://doi.org/10.1016/j.pocean.2009.03.004

Sampaio, E., Santos, C., Rosa, I. C., Ferreira, V., Pörtner, H.-O., Duarte, C. M., et al. (2021). Impacts of hypoxic events surpass those of future ocean warming and acidification. *Nature Ecology & Evolution*, *5*(3), 311–321. https://doi.org/10.1038/s41559-020-01370-3

Sasaki, H., Nonaka, M., Masumoto, Y., Sasai, Y., Uehara, H., & Sakuma, H. (2008). An Eddy-Resolving Hindcast Simulation of the Quasiglobal Ocean from 1950 to 2003 on the Earth Simulator. In K. Hamilton & W. Ohfuchi (Eds.), *High Resolution Numerical Modelling of the Atmosphere and Ocean* (pp. 157–185). New York, NY: Springer. https://doi.org/10.1007/978-0-387-49791-4_10

Sasano, D., Takatani, Y., Kosugi, N., Nakano, T., Midorikawa, T., & Ishii, M. (2015). Multidecadal trends of oxygen and their controlling factors in the western North Pacific. *Global Biogeochemical Cycles*, *29*(7), 935–956. https://doi.org/10.1002/2014GB005065

Sasano, D., Takatani, Y., Kosugi, N., Nakano, T., Midorikawa, T., & Ishii, M. (2018). Decline and Bidecadal Oscillations of Dissolved Oxygen in the Oyashio Region and Their Propagation to the Western North Pacific. *Global Biogeochemical Cycles*, *32*(6), 909–931. https://doi.org/10.1029/2017GB005876

Schmidtko, S., Stramma, L., & Visbeck, M. (2017). Decline in global oceanic oxygen content during the past five decades. *Nature*, *542*(7641), 335–339. https://doi.org/10.1038/nature21399

Sharp, J. D., Fassbender, A. J., Carter, B. R., Johnson, G. C., Schultz, C., Dunne, J. P. (2022). GOBAI-O_2: A Global Gridded Monthly Dataset of Ocean Interior Dissolved Oxygen Concentrations Based on Shipboard and Autonomous Observations (NCEI Accession 0259304). NOAA National Centers for Environmental Information. Dataset. https://doi.org/10.25921/z72m-yz67.

Sharp, J. D., Fassbender, A. J., Carter, B. R., Johnson, G. C., Schultz, C., & Dunne, J. P. (2023). GOBAI-O_2: temporally and spatially resolved fields of ocean interior dissolved oxygen over nearly 2 decades. *Earth System Science Data*, *15*(10), 4481–4518. https://doi.org/10.5194/essd-15-4481-2023

Stramma, L., Schmidtko, S., Bograd, S. J., Ono, T., Ross, T., Sasano, D., & Whitney, F. A. (2020). Trends and decadal oscillations of oxygen and nutrients at 50 to 300 m depth in the equatorial and North Pacific. *Biogeosciences*, *17*(3), 813–831. https://doi.org/10.5194/bg-17-813-2020

Stramma, L., & Schmidtko, S. (2021). Tropical deoxygenation sites revisited to investigate oxygen and nutrient trends. *Ocean Science*, *17*(3), 833–847. https://doi.org/10.5194/os-17-833-2021

Suga, T., Takei, Y., & Hanawa, K. (1997). Thermostad Distribution in the North Pacific Subtropical Gyre: The Central Mode Water and the Subtropical Mode Water. Retrieved from https://journals.ametsoc.org/view/journals/phoc/27/1/1520-0485_1997_027_0140_tditnp_2.0.co_2.xml

Suga, T., Motoki, K., Aoki, Y., & Macdonald, A. M. (2004). The North Pacific Climatology of Winter Mixed Layer and Mode Waters. Retrieved from https://journals.ametsoc.org/view/journals/phoc/34/1/1520-0485_2004_034_0003_tnpcow_2.0.co_2.xml

Takatani, Y., Sasano, D., Nakano, T., Midorikawa, T., & Ishii, M. (2012). Decrease of dissolved oxygen after the mid-1980s in the western North Pacific subtropical gyre along the 137°E repeat section. *Global Biogeochemical Cycles*, *26*(2). https://doi.org/10.1029/2011GB004227

Takeshita, Y., Martz, T. R., Johnson, K. S., Plant, J. N., Gilbert, D., Riser, S. C., et al. (2013). A climatology-based quality control procedure for profiling float oxygen data. *Journal of Geophysical Research: Oceans*, *118*(10), 5640–5650. https://doi.org/10.1002/jgrc.20399

Udaya Bhaskar, T. V. S., Sarma, V. V. S. S., & Pavan Kumar, J. (2021). Potential Mechanisms Responsible for Spatial Variability in Intensity and Thickness of Oxygen Minimum Zone in the Bay of Bengal. *Journal of Geophysical Research: Biogeosciences*, *126*(6), e2021JG006341. https://doi.org/10.1029/2021JG006341

Winkler, L. W. (1888). Die Bestimmung des im Wasser gelösten Sauerstoffes. *Berichte Der Deutschen Chemischen Gesellschaft*, *21*(2), 2843–2854. https://doi.org/10.1002/cber.188802102122

Wolf, M. K., Hamme, R. C., Gilbert, D., Yashayaev, I., & Thierry, V. (2018). Oxygen Saturation Surrounding Deep Water Formation Events in the Labrador Sea From Argo-O_2 Data. *Global Biogeochemical Cycles*, *32*(4), 635–653. https://doi.org/10.1002/2017GB005829

Yasuda, I. (2004). North Pacific Intermediate Water: Progress in SAGE (SubArctic Gyre Experiment) and Related Projects. *Journal of Oceanography*, *60*(2), 385–395. https://doi.org/10.1023/B:JOCE.0000038344.25081.42

You, Y. (2003). The pathway and circulation of North Pacific Intermediate Water. *Geophysical Research Letters*, *30*(24). https://doi.org/10.1029/2003GL018561

887

888